

# Physics Informed Neural Network Framework for Unsteady Discretized Reduced Order System

Rahul Halder<sup>\*1</sup>, Giovanni Stabile<sup>†2</sup>, and Gianluigi Rozza<sup>‡1</sup>

<sup>1</sup>Mathematics Area, mathLab, SISSA, via Bonomea 265, I-34136 Trieste, Italy

<sup>2</sup>Department of Pure and Applied Sciences, Informatics and Mathematics Section, University of Urbino Carlo Bo, Piazza della Repubblica, 13, I-61029 Urbino, Italy

## ABSTRACT

This work addresses the development of a physics-informed neural network (PINN) with a loss term derived from a discretized time-dependent reduced-order system. In this work, first, the governing equations are discretized using a finite difference scheme (whereas, any other discretization technique can be adopted), then projected on a reduced or latent space using the Proper Orthogonal Decomposition (POD)-Galerkin approach and next, the residual arising from discretized reduced order equation is considered as an additional loss penalty term alongside the data-driven loss term using different variants of deep learning method such as Artificial neural network (ANN), Long Short-Term Memory based neural network (LSTM). The LSTM neural network has been proven to be very effective for time-dependent problems in a purely data-driven environment. The current work demonstrates the LSTM network's potential over ANN networks in physics-informed neural networks (PINN) as well. The major difficulties in coupling PINN with external forward solvers often arise from the inability to access the discretized forms of the governing equation directly through the PINN solver and also to include those forms in the computational graph of the network. This poses a significant challenge especially when a gradient-based optimization approach is considered in the neural network. Therefore, we propose an additional step in the PINN algorithm to overcome these difficulties. The proposed methods are applied to a pitch-plunge airfoil motion governed by rigid-body dynamics and a one-dimensional viscous Burgers' equation. The potential of using discretized governing equations instead of continuous form lies in the flexibility of input to the PINN. The current work also demonstrates the prediction capability of various discretized-physics-informed neural networks outside the domain where the data is available or governing equation-based residuals are minimized.

**Keywords:** Reduced Order Model (ROM), Proper Orthogonal Decomposition (POD)-Galerkin Projection, Discretized Partial Differential Equation (PDE), Physics Informed Neural Network (PINN), Long Short Term Memory (LSTM) Network.

## 1 Introduction

Reduced order modelling [37, 32, 7] for computational physics problems has gained significant research focus in the past few decades. Usually, the computational effort of reduced-order model development involves two distinct stages - one is the offline stage where the high-fidelity simulation datasets are generated using high-performance computing (HPC) and the other one is the online stage which is performed using comparatively less powerful machines. Based on the learning methodology of the parametric space or unsteady dynamics, the reduced order model can be broadly classified into two categories, i.e. intrusive and non-intrusive reduced order model. In the intrusive approach, the governing equations are first projected on a reduced space, and the resulting equations are solved numerically as a time-marching problem on the reduced space. Therefore, the

---

<sup>\*</sup>rhalder@sisssa.it

<sup>†</sup>giovanni.stabile@uniurb.it

<sup>‡</sup>grozza@sisssa.it

intrusive schemes require significant modification of the solver whereas the non-intrusive reduced order model, on the other hand, is entirely data-driven and a surrogate model is generated with a database from a high-fidelity numerical or experimental dataset. Therefore, the second approach requires minimal changes in the computational solver.

The projection-based intrusive reduced order model often possesses numerical stability issues if the solution manifold is highly nonlinear, requiring a large dimension of the linear subspace used to approximate the solution manifold and increasing the computational cost of the reduced order schemes. Among several intrusive reduced-order model approaches, POD-Galerkin-based ROM [41, 27, 40, 42], has been very effective in approximating the dynamics in a low dimensional manifold. A survey of projection-based ROM for parameterized dynamical systems is carried out by Benner et al. [6]. An additional effort is required in the projection-based intrusive ROM approach to handle the nonlinear term requiring several hyper-reduction methods [3, 10, 9, 20]. Since in an intrusive ROM framework, the governing equations are satisfied in the reduced or latent space, this type of ROM is expected to produce accurate prediction even at a sparse training dataset.

There have been several progresses in non-intrusive reduced order model in recent times [5, 15, 16, 21]. For ill-posed problems such as inverse, regression, and classification problems in diverse fields of computational mechanics, as outlined in Schmidhuber et al., [39], several deep learning (DL) approaches offer effective solutions. Maulik and San [30] and Duraisamy et al. [31] proposed a turbulence closure model using machine learning. Among other notable applications of deep learning in fluid mechanics problems are the combined proper orthogonal decomposition (POD) and LSTM network for incompressible flows with spectral proper orthogonal decomposition (SPOD) of Wang et al. [44] and the application of a dimensionality reduction method with DL networks for learning feature dynamics from noisy data sets in Lui and Wolf [29]. As mentioned, non-intrusive approaches often require a large data set to gain significant prediction accuracy. LSTM network has been applied to several fields of computational physics problems such as aeroelastic applications and hydrodynamic applications by Halder et al. [23, 25], for the application in atmospheric turbulence by Rahman et al. [33]. However, such approaches, being completely data-driven or black-box methods, require large training datasets computed in the expensive offline stage, and thereby they appear to be ineffective in those application areas where sparse datasets are available. Hence, in the non-intrusive framework, a grey-box approach where the governing dynamics or the parametric space can be learnt from the governing equations in addition to data-driven constraints can circumvent the requirement of a large training dataset.

In the past century, early work on solving partial differential equations (PDE) using neural networks starts with Dissanayake and Phan-Thien [18]. With recent advancements in research of neural networks, this topic got renewed attention with the work of Raissi et al. [34]. Physics-informed neural networks can circumvent the problem of large training dataset requirements by introducing additional physics-based loss terms. This physics-based loss term in neural networks can be computed from the governing equations. Different types of neural networks can be considered in the context of PINN, such as artificial neural networks (ANN) by Raissi et al. [34], Waheed et al. [8], Tartakovsky et al. [43] and Schiassi et al. [38]. Similarly, Gao et al. [22] and Fang [19] coupled convolution neural networks (CNN) with physics constraints. A review of several developments in PINN is summarized by Cuomo et al. [14]. However, there are limited works in Physics Informed Long Short-Term Neural Network (LSTM). Zhang et al. [12] used a tensor differentiator to determine the derivatives of state space variables to couple the LSTM network with physics information arising from the governing equations and applied to nonlinear-structural problems. PINN usually considers an automatic differential (AD) based approach [4] for the computation of the gradients. There have been few efforts to use derivatives based on known numerical approaches such as finite difference, finite-element, finite volume methods etc. to compute the physics-driven loss-term in the PINN network. Ranade et al. [35] proposed a Discretization-net where finite volume-based numerical residuals are considered in the loss term of the physics-informed neural network. Similar work by Aulakh et al. [2] coupled physics-informed ANN network with the finite volume-based discretization of the OpenFOAM solver. The PINN network often takes more time than the forward solvers due to the large dimensionality of the network output. To reduce this effort the governing equation can be first reduced using the conventional dimensionality reduction approach, such as Proper Orthogonal Decomposition (POD), and then can be coupled with the loss equations as shown by Chen et al. [11] and Hijazi et al. [26]. The full potential of the discretized physics-based neural network will be realized if one can couple the PINN solver and the external forward solver each independently formulated within distinct coding environments. In such a

case, none of the previous works propose a seamless coupling of the external solver with the PINN environment without further modification of the forward solver. **Discretized governing equation augmented LSTM network is demonstrated for the first time by the author [25]**, but the detailed comparison of prediction accuracy in the context of different neural networks and extension of the algorithm to a spatiotemporal problem will be demonstrated in the present work.

The contribution of the current work can be summarized as follows:

- The current work proposes a novel approach where the existing forward solvers can be used in the PINN framework. Therefore, the solvers can be used for ill-posed and inverse problems. In the present work, although we have coupled the PINN environment with a PyTorch-based external numerical solver, the motivation of the current work is to bridge the PINN environment with the existing C++-based open-source solvers for handling complex geometry and more practical applications as a future endeavour.
- Current work proposes discretized governing equations based LSTM-PINN network for unsteady spatio-temporal problems of interest for the first time as per authors' knowledge.
- Detail studies of prediction and reconstruction capabilities involving several neural networks such as ANN and LSTM and discretized governing equations are carried out.
- The PINN network often suffers from the large-dimensionality of problems. Therefore, we propose to use the projection-based ROM framework used in [41] in the PINN platform to accelerate the training time.
- we propose an augmentation of the Physics-Informed Neural Network (PINN) algorithm, which incorporates an additional step to seamlessly integrate with any external solver. This additional step will eliminate the necessity for the incorporation of the discretized form of the governing equation within the computational graph of the neural network.

The current paper is organized in the following way.

- First, in section 2, the general formulation of the discretized governing equation is presented, followed by the reduced-order representation of the discretized equation discussed.
- Next, in section 3, the architecture of the ANN and LSTM network and their extension to a physics-informed neural network using additional loss penalty arising from the numerical residual of the reduced order discretized equations are discussed. In this section, we also discuss the software implementations [17] details of the work.
- Furthermore, we propose an additional step of importing the physics-based residual and the Jacobian of the residual vector with respect to the output variable in the PINN solver if the external CFD solver is completely detached from the PINN environment to facilitate the inclusion of the discretized form of equation in the computational graph of the neural network.
- Finally, in section 4, the proposed approaches are applied in the context of a 2-dof linear structural equation and a viscous Burgers' equation (full order and reduced order) to demonstrate the discretized physics-informed ANN and LSTM network. Next, in the context of the full-order Burgers' equation, we demonstrate our additional step of the PINN algorithm for seamless coupling of two separate environments - PINN solver and external forward solver.

## 2 Governing Equations and Reduced Order System

The governing equations associated with different computational mechanics' problems can be cast into the general form of a nonlinear parameterized dynamical system as shown in Equation 1

$$\frac{\partial u(t; \mu)}{\partial t} = \mathbf{A}(\mu)u(t; \mu) + \mathbf{F}(u; \mu; t)u(t; \mu) + \mathbf{B}(\mu)f(\mu), \quad u(0; \mu) = u^0(\mu), \quad (1)$$

where,  $\mu \in \Omega_\mu \subset \mathbb{R}^{N_\mu}$  is a vector containing the parameters associated with the dynamical system,  $u : [0, T] \times \mathbb{R}^{N_\mu} \rightarrow \mathbb{R}^N$  denotes the time-dependent state variable function.  $u^0 : \mathbb{R}^{N_\mu} \rightarrow \mathbb{R}^N$  is the initial state.  $f : [0, T] \times \mathbb{R}^{N_\mu} \rightarrow \mathbb{R}^{N_i}$  denotes the time-dependent input variable function

independent of the state variable function.  $N$ ,  $N_i$  and  $N_\mu$  are the number of degrees of freedom of high-fidelity solution, dimensions of the input variable and the parameter space respectively. The constant real-valued operator  $\mathbf{A} : \mathbb{R}^{N_\mu} \rightarrow \mathbb{R}^{(N \times N)}$  contributes to the linear part of the governing equation and the operator  $\mathbf{F} : \mathbb{R}^{N_\mu} \rightarrow \mathbb{R}^{(N \times N)}$  associated with the nonlinear part of the governing equation is dependent on the state variable. The operator  $\mathbf{B} : \mathbb{R}^{N_\mu} \rightarrow \mathbb{R}^{(N_i \times N_i)}$  associated with the input variable can also be dependent on the state variable based on the nature of the governing equation. Although, any time integration method can be adopted to time-discretize the dynamical system Equation 1, we show a backward Euler time-discretization with an implicit approach as the numerical schemes for the demonstration purpose, and the  $\mathbf{B}$  matrix is considered here to be independent of the state variables.

$$(I_N - \Delta t^{(k)} \mathbf{A}(\mu) - \Delta t^{(k)} \mathbf{F}(u^{(k)}; \mu; t))u^{(k)} = u^{(k-1)} + \Delta t^{(k-1)} \mathbf{B}(\mu; t)f(\mu), \quad (2)$$

whereas if we consider the explicit numerical discretization approach,

$$u^{(k)} = u^{(k-1)} + (\Delta t^{(k-1)} \mathbf{A}(\mu) + \Delta t^{(k-1)} \mathbf{F}(u^{(k-1)}; \mu; t))u^{(k-1)} + \Delta t^{(k-1)} \mathbf{B}(\mu; t)f(\mu), \quad (3)$$

where,  $I_N$  denotes the identity matrix of size  $\mathbb{R}^{(N \times N)}$ ,  $\Delta t$  is the time step and  $k$  denotes the  $k^{th}$  time instant. The following subsection will discuss the reduced-order formulation of the discretized governing equations.

## 2.1 Linear subspace solution representation

The computational complexity of Equation 2 and Equation 3 is of order  $\mathcal{O}(N)$ . Therefore, to reduce the computational effort of the full-order system, the state variables can be represented as the linear combination of a few basis vectors  $\Phi$  and the projected equation can be solved in a similar time-marching way as considered for the full-order model solution. We will propose in the following section 3 how we can solve the set of reduced-order equations in an alternative way in the context of physics-informed neural network. To find the basis vectors from a set of solution vectors associated with parameters  $\mu$ :

$$u(\mu) \approx \tilde{u}(\mu) \equiv \Phi \hat{u}(\mu), \quad (4)$$

where,  $\hat{u}(\mu) : \mathbb{R}^{N_\mu} \rightarrow \mathbb{R}^n$  with  $n \ll N$ . The basis vector sets  $\Phi \in \mathbb{R}^{N \times n}$  are defined as :

$$\Phi = [\phi_1 \quad \dots \quad \phi_2 \quad \dots \quad \phi_n]. \quad (5)$$

To compute the basis vector sets, we collect the solution vectors  $u$  at different time instants associated with the set of  $m$  parameter values  $[\mu_1, \mu_2, \dots, \mu_m]$ . At parameter  $\mu_p$ , the snapshot vectors associated with total time instants of  $N_t$  are defined as  $U_p = [u^{(1)}(\mu_p), u^{(2)}(\mu_p), \dots, u^{(N_t)}(\mu_p)] \in \mathbb{R}^{(N \times N_t)}$ . Now, if we concatenate the snapshots corresponding to all the parameters, we obtain the total snapshot matrix  $U \equiv [U_1 \quad \dots \quad U_{N_\mu}]$ , where  $U \in \mathbb{R}^{(N \times mN_t)}$ .

Proper Orthogonal Decomposition (POD) [41] can be used to compute the spatial basis vectors  $\Phi$  by choosing the first  $n$  columns of the left singular value matrix  $W$  after the application of Singular Value Decomposition (SVD) on the snapshot matrix  $U$  as shown in Equation 6.

$$\begin{aligned} U &= W \Sigma V^T, \\ &= \sum_{i=1}^l (\sigma_i w_i v_i^T), \end{aligned} \quad (6)$$

where  $l = \min(N, mN_t)$  and  $n < mN_t$ . Here,  $W \in \mathbb{R}^{N \times l}$  and  $V \in \mathbb{R}^{mN_t \times l}$  are set of orthogonal vectors and  $\Sigma \in \mathbb{R}^{l \times l}$  is a diagonal matrix where its diagonal elements consist of the singular values. The POD basis  $\Phi$  minimizes  $\|U - \Phi \Phi^T U\|_F$  where  $\|\cdot\|_F$  denotes the Frobenius norm. The reduced-order system of equations can be written from the Equation 2

$$\begin{aligned} (\Phi^T I_N \Phi - \Delta t^{(k)} \Phi^T \mathbf{A}(\mu) \Phi - \Delta t^{(k)} \Phi^T \mathbf{F}(\hat{u}^{(k)}; \mu; t) \Phi) \hat{u}^{(k)} = \\ \hat{u}^{(k-1)} + \Delta t^{(k)} \Phi^T \mathbf{B}(\mu; t) f(\mu), \end{aligned} \quad (7)$$

which can be written as follows:

$$(I_n - \Delta t^{(k)} A_R(\mu) - \Phi^T F(\Phi \hat{u}^{(k)}, \mu, t) \Phi \hat{u}^{(k)} = \hat{u}^{(k-1)} + \Delta t^{(k)} B(\mu; t) f(\mu), \quad (8)$$

where,  $A_R = \Phi^T A(\mu) \Phi$ . Furthermore, the reduced order system can be derived from the explicit formulation as shown in Equation 3. Similar to linear projection approaches such as Proper Orthogonal Decomposition (POD) as mentioned here, one can consider nonlinear manifold-based projection as shown by [36] using the Convolutional Autoencoders approach.

## 2.2 Test Cases

As mentioned earlier, the current work considers two test cases: the rigid body dynamical system for 2-dof pitch-plunge airfoil and the viscous Burgers' equation to demonstrate the proposed methodologies.

**(a) 2-dof pitch-plunge System** An implicit second-order backward Euler time discretization approach is considered to discretize the mass-spring system. The governing equation of the mass-spring system can be written as follows:

$$\begin{bmatrix} 1 & x_\alpha \\ x_\alpha & r_\alpha^2 \end{bmatrix} \begin{pmatrix} \ddot{h} \\ \ddot{\alpha} \end{pmatrix} + \begin{bmatrix} (\omega_h/\omega_\alpha)^2 & 0 \\ 0 & r_\alpha^2 \end{bmatrix} \begin{pmatrix} h \\ \alpha \end{pmatrix} = \frac{V^{*2}}{\pi} \begin{pmatrix} -Cl \\ -2Cm_{EA} \end{pmatrix}. \quad (9)$$

The terms  $x_\alpha$ ,  $r_\alpha$ ,  $\omega_h$ ,  $\omega_\alpha$  are structural variables as mentioned in Halder et al.[24].  $h$  and  $\alpha$  are the plunge and pitch degrees of freedom, respectively, and  $C_l$  and  $C_m$  are the lift and moment coefficient about the elastic axis [24] typically used for aeroelastic applications. The governing Equation 9 can be written as follows in matrix format:

$$\mathbf{M}\ddot{\mathbf{X}} + \mathbf{K}\mathbf{X} = \mathbf{F}, \quad (10)$$

where,  $\mathbf{M}$  and  $\mathbf{K}$  are the mass and stiffness matrix and the variable  $\mathbf{X}$  is  $[h \ \alpha]^T$  and  $\mathbf{f}$  is force matrix arising from Equation 9 respectively. The residual computed from Eqns. Equation 9 and Equation 10 can be written as follows:

$$\begin{aligned} r_{\text{rigid-body}} = & \frac{3 \left\{ \begin{matrix} X \\ \dot{X} \end{matrix} \right\}^{n+1} - 4 \left\{ \begin{matrix} X \\ \dot{X} \end{matrix} \right\}^n + \left\{ \begin{matrix} X \\ \dot{X} \end{matrix} \right\}^{n-1}}{2dt} \\ & + \begin{bmatrix} 0 & 0 & -1 & 0 \\ 0 & 0 & 0 & -1 \\ M^{-1}K & 0 & 0 & 0 \end{bmatrix} \left\{ \begin{matrix} X \\ \dot{X} \end{matrix} \right\}^{n+1} - \begin{bmatrix} 0 \\ 0 \\ M^{-1}F \end{bmatrix}^{n+1}. \end{aligned} \quad (11)$$

For the rigid-body dynamical systems, the number of dof is 2 and therefore, it does not require any further spatial reduction using Equation 4.

**(b) Viscous Burgers' Equation** An explicit discretization of the Burgers' equation with an upwind scheme for the convective term, the central difference scheme for the diffusion terms, and a forward difference scheme for the time derivative term is considered. For a given field  $u(x, t)$  and kinematic viscosity  $\nu$ , the general form of the Burgers' equation can be written as  $\frac{\partial u}{\partial t} + u \frac{\partial u}{\partial x} = \nu \frac{\partial^2 u}{\partial x^2}$ . The residual arising from the governing equation after discretization is as Equation 12

$$r_{\text{burgers}} = \frac{u_i^{n+1} - u_i^n}{dt} - u_i^n \frac{(u_{i+1}^n) - (u_i^n)}{dx} + \nu \frac{u_{i+1}^n - 2u_i^n + u_{i-1}^n}{(dx)^2}, \quad (12)$$

The residual,  $r_{\text{burgers}}$  can be expressed using a reduced order variable  $\hat{u}$ :

$$r_{\text{burgers, reduced}} = \frac{\hat{u}_i^{n+1} - \hat{u}_i^n}{dt} - \Phi^T \Phi \hat{u}_i^n \frac{(\Phi \hat{u}_{i+1}^n) - (\Phi \hat{u}_i^n)}{dx} + \nu \frac{\hat{u}_{i+1}^n - 2\hat{u}_i^n + \hat{u}_{i-1}^n}{(dx)^2}, \quad (13)$$

where  $dt$  and  $dx$  are the time-step and spatial discretization steps suitable for the numerical discretization approach in the current test case, and  $\nu$  is the viscosity coefficient.

### 2.3 Hyper Reduction

As demonstrated by Chaturantabut et al.[10], the complexity of the nonlinear term is not reduced in Equation 8. The nonlinear part of the reduced order equation can be written as :

$$\tilde{\mathbf{N}}(\hat{u}) := \underbrace{\Phi^T}_{n \times N} \underbrace{\mathbf{F}_{\mathbf{nl}}(\Phi \hat{u}(t, \mu))}_{N \times 1}. \quad (14)$$

where the nonlinear term  $\mathbf{F}_{\mathbf{nl}} = F(\Phi \hat{u}, \mu, t) \Phi \hat{u}$ . The nonlinear term has a computational complexity of  $(\mathcal{O}(\alpha(N) + 4Nn))$ , where  $\alpha$  is some function of  $N$ . Empirical Interpolation Method (EIM) as proposed by Barrault et al.[3], is a popular hyper-reduction approach to reduce the computational complexity of the nonlinear term. Hence in the current work, a variant of EIM approach, Discrete Empirical Interpolation Method (DEIM) as mentioned by Chaturantabut and Sorensen [10] is adapted to handle the nonlinear term. However, any other hyper-reduction approach such as the GNAT method by Carlberg et al.[9], the ECSW method by Farhat et al.[20] can also be considered. In the hyper-reduction approaches, the nonlinear term,  $\mathbf{F}_{\mathbf{nl}}(t, \mu)$  can be reconstructed from the information at a few collocation points in the computational domain. First, the nonlinear term  $\mathbf{F}_{\mathbf{nl}}(t, \mu)$  can first be projected on a subspace which approximates the space generated by the nonlinear term and spanned by the basis of dimension  $m_h \ll N$ . The basis vector sets  $\Phi^h = \{\phi^h_1, \dots, \phi^h_{m_h}\}$ . The nonlinear term then  $\mathbf{F}_{\mathbf{nl}}$  can be approximated as  $\mathbf{F}_{\mathbf{nl}}(t, \mu) = \Phi^h \mathbf{c}(t, \mu)$ , where the coefficient vector  $\mathbf{c}(t, \mu)$  can be computed from an index matrix or mask matrix  $\mathbf{P}$  used for indexing sensor locations in the computational domain. The index matrix is defined as  $\mathbf{P} = [e_{\rho 1}, \dots, e_{\rho l}] \in \mathbb{R}^{N \times m}$  where,  $\mathbf{e}_{\rho i} = [0, \dots, 0, 1, 0, \dots, 0]^T \in \mathbb{R}^N$ . 1 is placed at the  $i^{th}$  entry of the  $\mathbf{e}_{\rho i}$  vector.  $\mathbf{P}$  can be computed using the following relationship in Equation 15:

$$\mathbf{P}^T \mathbf{F}_{\mathbf{nl}}(\hat{u}, t, \mu) = (\mathbf{P}^T \Phi^h) \mathbf{c}(t, \mu), \quad (15)$$

and, the nonlinear term  $\mathbf{F}_{\mathbf{nl}}(t, \mu)$  can be approximated as follows:

$$\mathbf{F}_{\mathbf{nl}}(t, \mu) = \Phi^h (\mathbf{P}^T \Phi^h)^{-1} \mathbf{P}^T \mathbf{F}_{\mathbf{nl}}(\hat{u}, t, \mu), \quad (16)$$

$\mathbf{P}^T \mathbf{F}_{\mathbf{nl}}(t, \mu)$  indicates the location of the computational domain where the nonlinear term needs to be computed. Therefore, to reduce the computational complexity, the final nonlinear term to be used in the reduced form of the discretized Equation 13 can be written as follows:

$$\tilde{\mathbf{N}}(\hat{u}) = \Phi^T \Phi^h (\mathbf{P}^T \Phi^h)^{-1} \mathbf{P}^T \mathbf{F}_{\mathbf{nl}}(\hat{u}, t, \mu). \quad (17)$$

## 3 PINN for Discretized Reduced Order System

In this section, physics informed neural network using the discretized governing equation will be discussed. First, two different types of neural network architecture such as ANN and LSTM will be briefly introduced in subsection 3.1 followed by the integration with the discretized governing equation in the framework of the physics-informed neural network [34] which will be discussed in subsection 3.2 and subsection 3.3.

### 3.1 Neural Network Architecture

ANN formulates a nonlinear functional relationship between the input and output. In Equation 18,  $\mathbf{f}$  can be considered as input whereas the variable  $\mathbf{u}$  can be the output of the neural network and input-output mapping for a single-layer, ANN network can be written as follows:

$$\mathbf{u} = f_{\text{act}}(W\mathbf{f} + b), \quad (18)$$

where  $f_{\text{act}}$  is the nonlinear activation function. the weight matrix and  $b$  is the bias vector. In Equation 18, the input,  $\mathbf{f}$  and output  $\mathbf{u}$  can also correspond to an unsteady time series problem such as the mass-spring system and unsteady viscous Burgers' equation. The Eqn. Equation 18 can be rewritten as Equation 19:

$$p_o^{n_t} = f_{\text{act}}(W p_i^{n_t} + b), \quad (19)$$

where  $p_i^{n_t}$  corresponds to the input of the unsteady problem considered which is  $C_l$  and  $C_m$  at  $n_t^{th}$  time instant for the pitch-plunge airfoil and  $t$  for the Burgers' equation. Furthermore,  $p_o^{n_t}$  corresponds to the output of the unsteady problem considered which is  $h$  and  $\alpha$  at  $n_t^{th}$  time instant for the pitch-plunge airfoil and  $u$  at all the spatial locations for the Burgers' equation. However, in Recurrent Neural Networks (RNN), the output,  $p_o^{n_t}$  corresponds to the time history of the input instead of a single time instant value as shown in Equation 20. The other matrix  $U_R$  is not present in the architecture of ANN which is associated with the input from the previous time steps values and introduces the memory effect in the network architecture. In different variants of RNN,  $h_i^{(n_t)}$  forms a different functional relationship with previous time instant values of  $p_i$ . For a simple RNN network,  $h_i^{(n_t)} = p_i^{n_t-1}$

$$p_o^{n_t} = f_{act} \left( W p_i^{n_t} + U_R h_i^{(n_t)} + b \right). \quad (20)$$

The present work considers a variant of the RNN network called a Long Short Term Memory network (LSTM). A brief introduction to an LSTM cell and the associated network's input and output architecture will be briefly introduced now, which will be essential to understand the coupling between the LSTM network with the discretized PDE-based loss term, a topic of discussion in the following subsection. However, the advantages of the LSTM network over a simple RNN network, and the detailed architecture of the LSTM network can be found in Halder et al. [23, 25]. As mentioned, RNN-type neural networks require input values associated with a sequence of time instants. The output corresponds to the last time instant in the input time sequence. For example, for an input time-series,  $[x_1, x_2, x_3 \dots x_t]$ , corresponding output,  $[y_1, y_2, y_3 \dots y_t]$  and sequence length of  $s$  associated with the input, in the LSTM network,  $[x_1, x_2, \dots x_s]$  corresponds to output  $y_s$ . The input of the LSTM forms a tensor structure as shown in Figure 1a where the number of input variables attributed to the third dimension. For example, for a pitch-plunge airfoil system, the number of input variables is 2 which are  $C_l$  and  $C_m$  and for the Burgers' equation, time,  $t$  being the only input variable, its dimension is 1. Conversely, the output structure forms a matrix as shown in Figure 1b where the second dimension corresponds to the number of output variables. For a pitch-plunge airfoil system, the number of output variables is 2 which are  $h$  and  $\alpha$ , whereas, for the Burgers' equation the number of output variables is the number of spatial locations.

However, this input-output structure of both ANN and LSTM networks is adequate to understand the discretized reduced order system enhanced physics-informed neural network termed ANN-DisPINN and LSTM-DisPINN respectively which we will discuss in the following subsection 3.2 and subsection 3.3 .

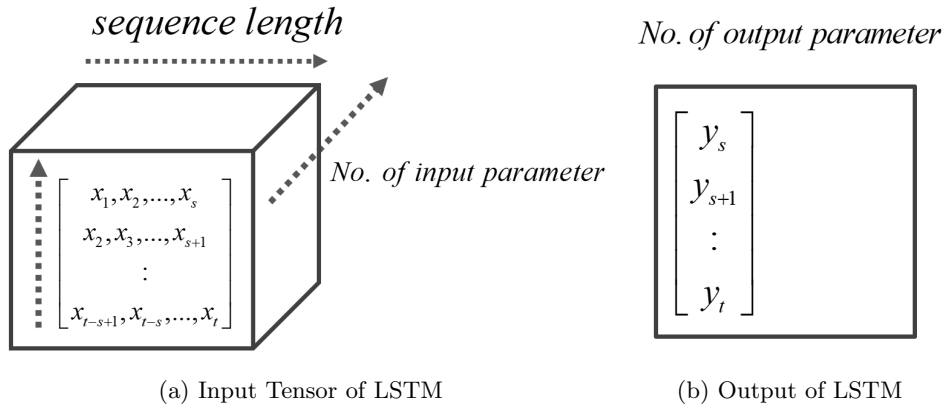


Figure 1: Input and output architecture of LSTM.

### 3.2 ANN-DisPINN

In this section, the discretized full-order or reduced-order governing equation is employed in the physics-informed neural network framework. The input and output structure of a simple ANN

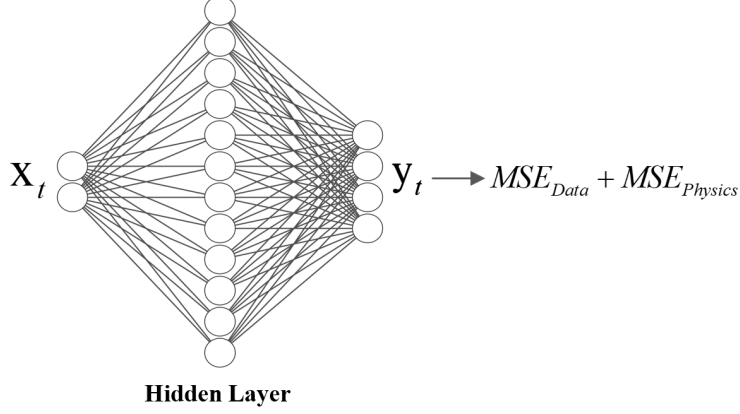


Figure 2: Architecture of ANN-DisPINN.

and ANN-Network is straightforward. For an unsteady problem,  $[x_1, x_2, x_3, \dots, x_t]$  is the input associated with different time instants and  $[y_1, y_2, y_3, \dots, y_t]$  are the output values corresponding to the inputs. Hence, a one-to-one correspondence exists between the input and output formulations associated with each time instant. However, in ANN-DisPINN proposed here in Figure 2, an additional loss penalty is introduced in addition to the data-driven loss part, which is coming from the discretized governing equation as shown in Equation 11 and Equation 13. The data-driven and physics-driven loss functions associated with the pitch-plunge airfoil and viscous Burgers' equation are as follows:

$$\begin{aligned} MSE_{Data} &= \|y_{\text{pred}} - y_{\text{actual}}\|_{L2}, \\ MSE_{\text{burgers}} &= \|r_{\text{burgers}}\|_{L2}, \\ MSE_{\text{rigid-body}} &= \|r_{\text{rigid-body}}\|_{L2}, \end{aligned} \quad (21)$$

where,  $y_{\text{pred}}$  is the predicted outcome from Equation 18 and  $y_{\text{actual}}$  is the benchmark numerical dataset available. The loss terms arising from the data-driven term  $MSE_{Data}$  and physics-driven term  $MSE_{\text{burgers}}$  and  $MSE_{\text{rigid-body}}$  need to be minimized to obtain the weight matrix  $W$  and bias vector  $b$  as mentioned in Equation 18 from this non-convex optimization problem statement which is inherent to the neural network algorithm. The 2-dof rigid body dynamical system does not require any spatial reduction whereas, the Burgers' equation is first projected on a reduced basis followed by residual computation from the reduced discretized equation which further serves as a loss penalty in the physics-driven loss term of ANN network as  $MSE_{\text{burgers-reduced}} = \|r_{\text{burgers-reduced}}\|_{L2}$

### 3.3 LSTM-DisPINN

As shown in Figure 1a, the input to the network is first re-formulated with a sequence length and then it is passed through the LSTM architecture as shown in Figure 3a and Figure 3b to obtain the  $y_{\text{pred}}$  from the nonlinear functional relationship between the input and output. It is clear from Figure 1b, we only obtain predicted output from  $s^{th}$  time step. The predicted  $y$  from the LSTM as shown in Figure 3b is further used to minimize the loss terms  $MSE_{Data}$ ,  $MSE_{\text{physics, burgers}}$  and  $MSE_{\text{physics, rigid-body}}$  to obtain the weight matrices and bias vectors associated with the LSTM network. Similarly, for the reduced order discretized system,  $MSE_{\text{physics, burgers-reduced}}$  should be considered in the physics-driven loss term.

The advantages of using the discretized system in the loss-term of the discretized-physics-informed neural networks are summarised below:

- The automatic differentiation (AD) based gradient computation [4] in conventional PINN framework requires the spatial coordinates (i.e., Cartesian coordinates) and time coordinates as the input to the neural network where the current approach provides a flexible choice of input.
- If a sparse numerical dataset is available to introduce in the data-drive loss term of the PINN network, they should comply with the numerical derivatives used in the physics-driven



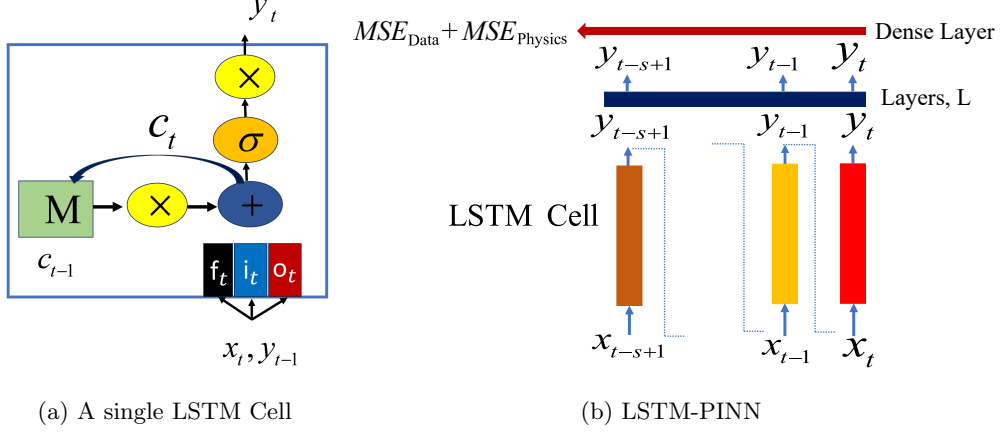


Figure 3: Architecture of a single LSTM-Cell and Discretized PDE-based LSTM-DisPINN.

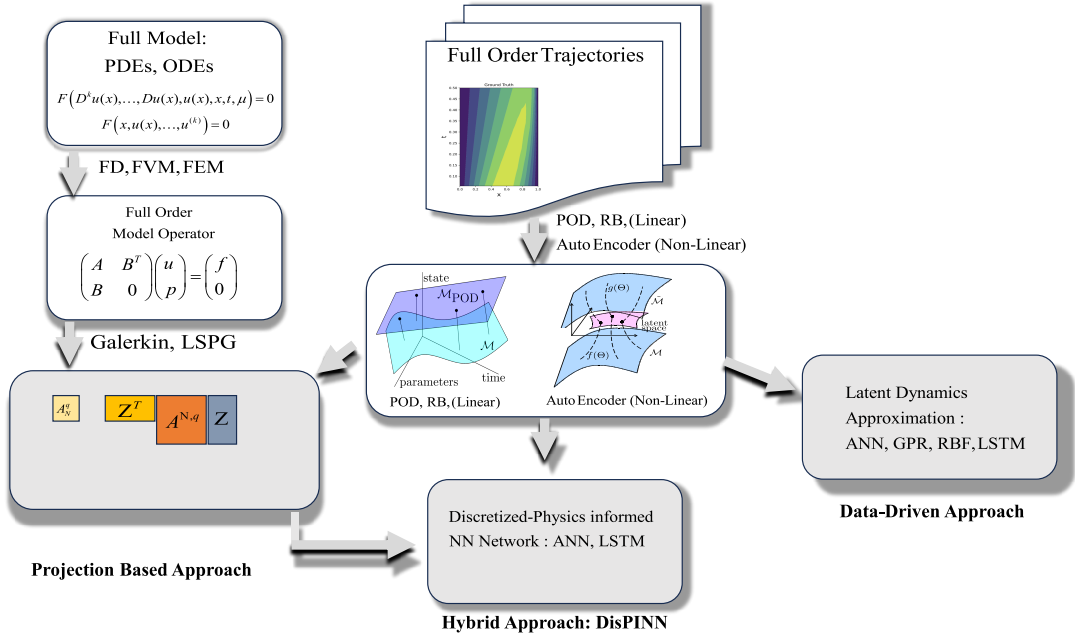


Figure 4: General framework for different reduced order models (i.e., projection-based approach, data-driven approach) and DisPINN, a bridge between these two aspects.

loss function, which have been used to generate those numerical datasets. However, in the conventional PINN framework, the numerical data often does not comply with the AD-based derivative resulting in a less accurate prediction.

The discretized-physics-based neural network(DisPINN) can be put in the context of a projection-based reduced order model and data-driven approach as shown in Figure 4. The implementation of the ANN-DisPINN and LSTM-DisPINN is carried out in the PyTorch-based PINN platform, PINA [13].

### 3.4 External Solver Coupling

Here we discuss the coupling procedure of PINN with the external solver detached from the computational graph in the neural network. In a conventional neural network framework, the derivative of the physics-based loss term ( $L_{\text{eqn}}$ ) and data-driven loss-term ( $L_{\text{Data}}$ ) concerning the neural network parameters,  $p = [W, b]$  is computed from the computational graph using backpropagation

algorithm as mentioned by Amari et al.[1]. The data-driven loss term is :

$$L_{\text{Data}} = \frac{1}{N_{\text{Data}}} \sum_{i=1}^{N_{\text{Data}}} (y_{\text{pred}} - y_{\text{actual}})^2 \quad (22)$$

Whereas the physics-driven loss term is :

$$L_{\text{eqn}} = \frac{1}{N_{\text{eqn}}} \sum_{i=1}^{N_{\text{eqn}}} R^2 \quad (23)$$

where, the physics-based residual,  $R$  can arise from full-order or reduced-order equations, such as  $r_{\text{burgers}}$ , reduced and  $r_{\text{burgers}}$ .  $N_{\text{Data}}$  and  $N_{\text{eqn}}$  is the number of points available for the computation of ( $L_{\text{Data}}$ ) and residual,  $R$  respectively. The derivative of  $L_{\text{eqn}}$  concerning the parameters can be computed as follows:

$$\partial L_{\text{eqn}} / \partial p = \left( \frac{1}{N_{\text{eqn}}} \sum_1^{N_{\text{eqn}}} 2R \frac{\partial R}{\partial p} \right) = \left( \frac{1}{N_{\text{eqn}}} \sum_1^{N_{\text{eqn}}} 2R \frac{\partial R}{\partial y_{\text{pred}}} \frac{\partial y_{\text{pred}}}{\partial p} \right) \quad (24)$$

Now, if the physics-based residual,  $R$  is computed from an external solver, it is very difficult to access the discretized form directly from the PINN solver, therefore we can not compute  $\partial L_{\text{eqn}} / \partial p$  from the computational graph using back-propagation. However if both the  $R$  and  $\frac{\partial R}{\partial U}$  are imported from the external solver, the modified physics-based loss term,  $L_{\text{Dis}}$  that can be passed through the backpropagation is written as follows:

$$L_{\text{Dis}} = \left( \frac{1}{N_{\text{eqn}}} \sum_1^{N_{\text{eqn}}} \left[ 2R \frac{\partial R}{\partial y_{\text{pred}}} \right]_{\text{detached}} y_{\text{pred}} \right) \quad (25)$$

Since, both the  $R$  and  $\frac{\partial R}{\partial U}$  are imported from the external solver, therefore detached from the computational graph, the derivative concerning the parameter is only computed on  $y_{\text{pred}}$ . Hence the loss term term which needs to be passed through the backpropagation is ( $L = L_{\text{Dis}} + L_{\text{Data}}$ ). Finally, a stochastic gradient descent approach is considered in the current work as mentioned in [1] to update the weight matrices and bias vectors based on  $\partial L / \partial p$  following the relationship:

$$p_{\text{new}} = p_{\text{old}} - \alpha \frac{\partial L}{\partial p} \quad (26)$$

where,  $p_{\text{new}}$  and  $p_{\text{old}}$  are the updated and old parameter values and  $\alpha$  is the learning rate. If the residual  $R$  is computed from the external solver, Jacobian,  $J = \frac{\partial R}{\partial y_{\text{pred}}}$  needs to be updated at every epoch. However,  $\frac{\partial R}{\partial y_{\text{pred}}}$  is a sparse matrix, and the overall computational expense of PINN solver can increase several folds if the  $J$  term is updated every epoch and it contains residual from the entire computational domain. Therefore the computational expenditure can be reduced by following steps.

- Jacobian term,  $J$  is updated only at a certain epoch interval.
- Residual,  $R$  is computed at collocation points in the spatial domain which is an outcome of the reduced order method as mentioned in section 2

In the current work, the  $J$  term is computed using finite-difference (FD), and no additional modification is required in the external solver, demonstrating the potential of our approach for seamless coupling of PINN with any other external forward solver. algorithm 1 summarize the proposed DisPINN in a pseudo-code. As indicated earlier, the primary inputs to the DisPINN algorithm are input to a prescribed neural network (NN),  $\mathbf{u}$ , the number of points for the computation of physics-based and data-driven loss terms as  $N_{\text{eqn}}$  and  $N_{\text{data}}$ . The iteration number in the optimization process is termed as *epoch*.  $k$  is the *epoch* interval at which the Jacobian,  $J$  is updated. The updated  $J$  after the prescribed interval is termed as  $J_{\text{new}}$ .

---

**Algorithm 1:** DisPINN pseudo-code for coupling external detached forward solver

---

```

Data:  $y_{\text{actual}}, \mathbf{u}, N_{\text{data}}, N_{\text{eqn}}$ 
1  $[W, b] \leftarrow \text{INIT}([W, b])$  ; /* Initialize Weight and bias */
2 while  $\text{epoch} \leq \text{Total Epoch No.}$  do
3    $y_{\text{pred}} \leftarrow \text{NN}(W, b, f_{\text{act}}, \mathbf{u})$  ; /* prediction from chosen network NN */
4    $\text{Ext. Solver} \leftarrow y_{\text{pred}}$  ; /* pass to external solver */
5    $R \leftarrow \text{Ext. Solver}$  ; /* pass to PINN solver from external solver */
6    $L_{\text{eqn}} \leftarrow \frac{1}{N_{\text{eqn}}} \sum_{i=1}^{N_{\text{eqn}}} R^2$  ; /* compute physics-based loss term */
7    $L_{\text{Data}} \leftarrow \frac{1}{N_{\text{data}}} \sum_{i=1}^{N_{\text{data}}} (y_{\text{pred}} - y_{\text{actual}})^2$  ; /* compute data-based loss term */
8   if  $\text{rem}(\text{epoch}, k) = 0$  then
9      $\frac{\partial R}{\partial y_{\text{pred}}} \leftarrow \text{Ext. Solver}$  ; /* compute Jacobian from external solver */
10     $J_{\text{new}} \leftarrow \frac{\partial R}{\partial y_{\text{pred}}}$  ;
11     $L_{\text{Dis}} \leftarrow (\frac{1}{N_{\text{eqn}}} \sum_{i=1}^{N_{\text{eqn}}} 2R J_{\text{new}} y_{\text{pred}})$  ; /* compute additional physics based
        loss term for backpropagation */
12  else
13     $J \leftarrow J_{\text{new}}$  ;
14     $L_{\text{Dis}} \leftarrow (\frac{1}{N_{\text{eqn}}} \sum_{i=1}^{N_{\text{eqn}}} 2R J y_{\text{pred}})$  ;
15   $L \leftarrow (L_{\text{Dis}} + L_{\text{Data}})$  ; /* compute total loss term for backpropagation */
16   $\Delta W \leftarrow -\alpha \text{G}_{\text{ADAM}}(\nabla_W L), \Delta b \leftarrow -\alpha \text{G}_{\text{ADAM}}(\nabla_b L)$  ;
    ; /* compute weight matrices and bias vector update */
17   $W \leftarrow W + \Delta W, b \leftarrow b + \Delta b$  ;

```

---

## 4 Numerical results

This section considers two unsteady test cases: an unsteady pitch-plunge airfoil motion under a sinusoidal excitation and an unsteady viscous Burgers' equation. We first discuss the details of the high-fidelity models, followed by the surrogate models, ANN-DisPINN and LSTM-DisPINN corresponding to both test cases in subsection 4.1 and subsection 4.2. Finally, the PINN network based on the reduced order discretized equation is demonstrated in the context of the viscous Burgers' equation in subsection 4.3. Since, in our current work, both the external solver and the PINN solver are developed in the PyTorch environment, it is not difficult to access the discretized form of the governing equation in the external solver from the PINN and include those forms in the computational graph for the computation of derivatives required for gradient descent optimization. However, in subsection 4.4, the output residual and the Jacobian are detached from the computational graph before they are passed to the PINN solver to implement algorithm 1 and application is demonstrated on the full-order Burgers' equation.

### 4.1 Mass-Spring System

To develop the high-fidelity numerical model and surrogate model for the pitch-plunge system, the structural properties, mentioned in Equation 9 are taken the same as those defined in [28, 25]. First, the dynamical system is excited with a sinusoidal input,  $\sin(10t)$  as  $C_l$  coefficient and  $\sin(20t)$  as  $C_m$  coefficient, whereas, the coefficient  $(V^2/\pi)$  describing the non-dimensionalized uniform air velocity is taken as 1. The time derivatives are computed with respect to the non-dimensional time  $\tau$ , where  $\tau = \omega_\alpha t$ .  $t$  is the dimensional time. In the current computation, the dimensional and non-dimensional time steps are  $\Delta t = \pi/1800$  and  $\Delta \tau = \pi/18$  respectively. The time derivatives are discretized using the second-order backward Euler scheme. Next, to develop the surrogate model, an ANN and an LSTM network are generated to map between the input which is  $C_l$  and  $C_m$  coefficient and the output,  $h$  and  $\alpha$ . 1000 time steps are considered for developing the neural networks. For the ANN network, 4 hidden layers are considered where the layers consist of 124, 64, 24 and 8 neurons respectively. The LSTM network, on the other hand, consists of a layer with 10 neurons in each LSTM cell. The sequence length of the LSTM cell is taken as 10. Furthermore, we also carry out the prediction of structural response, pitch and plunge using conventional PINN (ANN, with AD-based derivative). Here, the time instants,  $t$  need to be considered as input to

compute the temporal derivatives from the computational graph, in physics-based loss term derived from Equation 9. Temporal variation of the structural responses,  $h$  and  $\alpha$  at different time instants are considered as the output of the neural network. The hyper-parameters are the same as the ANN and LSTM networks, mentioned earlier. Therefore, We intend to carry out 5 different surrogate models such as a data-driven approach - ANN and LSTM, Conventional AD-based PINN, AD-PINN and our proposed ANN-DisPINN and LSTM-DisPINN. Figure 5 shows both physics-driven and data-driven  $MSE$  loss terms with the number of epochs.

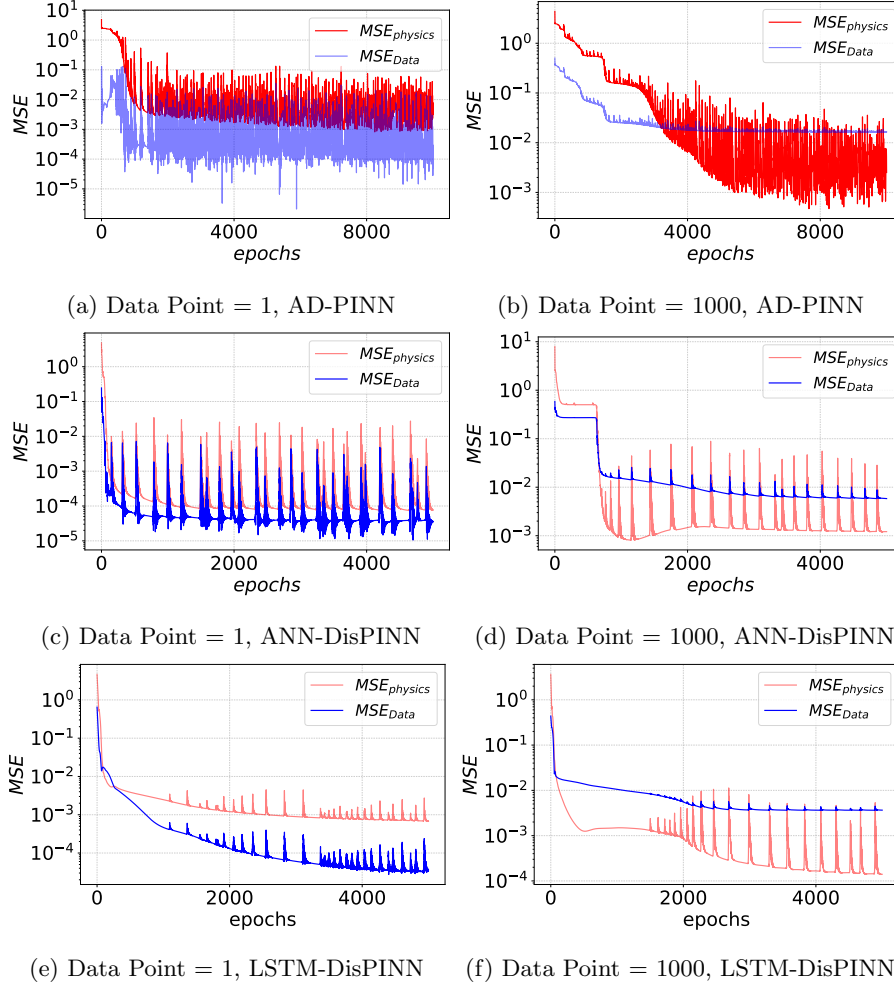


Figure 5: Data-driven and physics-driven loss term with no. of epochs for different physics-informed neural networks.

We demonstrate in Figure 5, that when conventional AD-PINN is used, the decay rate of the loss terms is slower than the discretized physics-based PINN, ANN-DisPINN and LSTM-DisPINN. Choice of input often contributes to the convergence of the  $MSE$  loss terms as shown by [17] where an extra forcing term in the input of the PINN accelerated the loss convergence. The  $C_l$  and  $C_m$  are the better choices as inputs in the case of the discretized-physics-based PINN as compared to the time,  $t$  as an input for the conventional AD-based PINN, since the input,  $C_l$  and  $C_m$  has the same frequency content similar to output  $h$  and  $\alpha$ . Furthermore, in the case of the discretized-physics-based PINN, the data-driven loss term of the PINN network is consistent with the numerical derivatives used in the physics-driven residual as indicated in section 3. Therefore, the physics-based loss term ( $MSE_{physics}$ ) and data-driven loss term ( $MSE_{Data}$ ) associated with the disPINN decays faster than the AD-based PINN. It is evident from Figure 5b, in the case of AD-PINN, that when the full dataset is used,  $MSE_{data}$  does not decay below  $10^{-2}$  due to the inconsistency of the physics-driven and data-driven loss term. However, with DisPINN while using the data points of 1000 as shown in Figure 5d and Figure 5f,  $MSE_{Data}$  has dropped below  $10^{-2}$ .

Figure 6 and Figure 7 compares the prediction of the pitch and plunge response using the

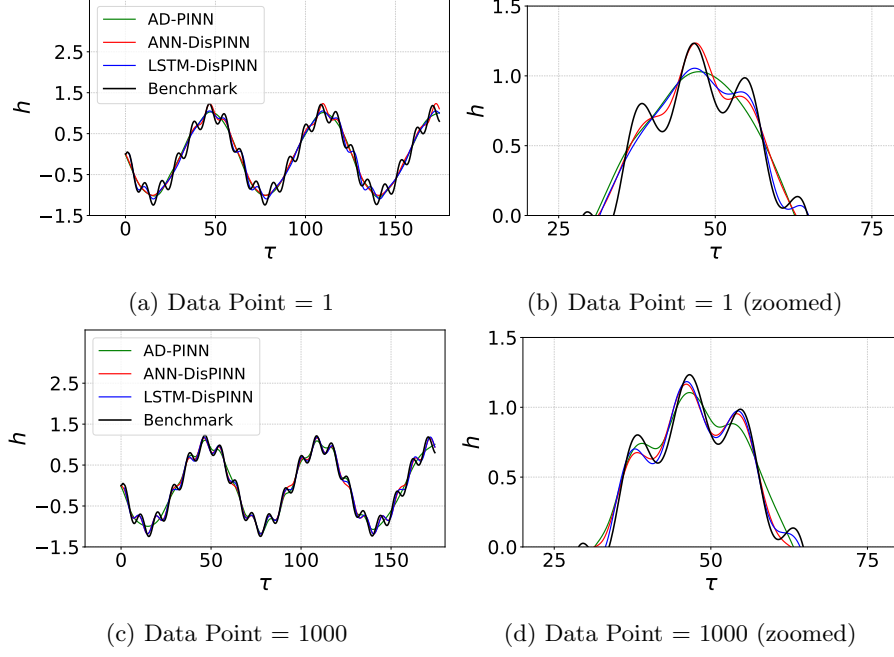


Figure 6: Comparison of the AD-PINN, LSTM-DisPINN and ANN-DisPINN prediction of the plunge response with benchmark numerical data

surrogate models i.e., the purely data-driven models such as ANN and LSTM, AD-based conventional PINN, AD-PINN and discretized physics-based PINN, ANN-DisPINN and LSTM-DisPINN networks with the high-fidelity benchmark results. The objective of the current exercise is to reconstruct the full unsteady response using only a few data points corresponding to different time instants in the structural responses. However, as mentioned in Equation 11, the residuals from the governing equations in the discretized form (for DisPINN) and continuous form (AD-PINN) are first obtained at all the time instants in the temporal domain using the neural network prediction such as shown in Equation 19 and Equation 20 at every iteration of the optimization algorithm used in the neural network. Next, the residuals are used as the physics-based loss penalty term in addition to the data-driven loss term in the PINN to obtain the corrected weight matrices and bias vectors. Since there are 1000 time instants in the temporal domain, in the ANN network, the input size consisting of sinusoidal  $C_l$  and  $C_m$  is  $\mathbb{R}^{(1000 \times 2)}$ . However, in the LSTM-DisPINN network, considering the sequence length of 10, the input tensor dimension is  $\mathbb{R}^{(990 \times 10 \times 2)}$ . Furthermore, the output dimension for the ANN-DisPINN and LSTM-DisPINN is  $\mathbb{R}^{(1000 \times 2)}$  and  $\mathbb{R}^{(990 \times 2)}$  consisting of the structural responses  $h$  and  $\alpha$  corresponding to the input  $C_l$  and  $C_m$  coefficients. Here, datasets of different sizes named as data points are randomly chosen from the temporal domain. In the PINN network, out of the 1000 training points mentioned above, only 1, 3, 200, and the entire dataset, 1000 are considered for the output prediction. These data points are different from the initial point, which are the first and 10<sup>th</sup> time instant in the temporal domain for the ANN and LSTM network, respectively. The ANN-DisPINN and the LSTM-DisPINN are capable of predicting the system responses significantly well even when only 1 data point is considered, as shown in Figure 6a and zoomed view in Figure 6b. AD-PINN, on the other hand, with fewer amount of data-points (i.e. 1), fails to reconstruct the small oscillations in the structural response as shown in Figure 6b. However, small oscillations in the pitch and plunge responses are well-captured with 1000 data points using both DisPINN and AD-PINN methods as shown in Figure 6c and zoomed view in Figure 6d. Similar trends are also visible in the case of pitch responses as well as shown in Figure 7.

Figure 8 shows the potential of the LSTM-DisPINN and ANN-DisPINN over pure data-driven ANN and LSTM networks and AD-PINN. The prediction errors at all the time instants using different data points are computed in the following Equation 27.

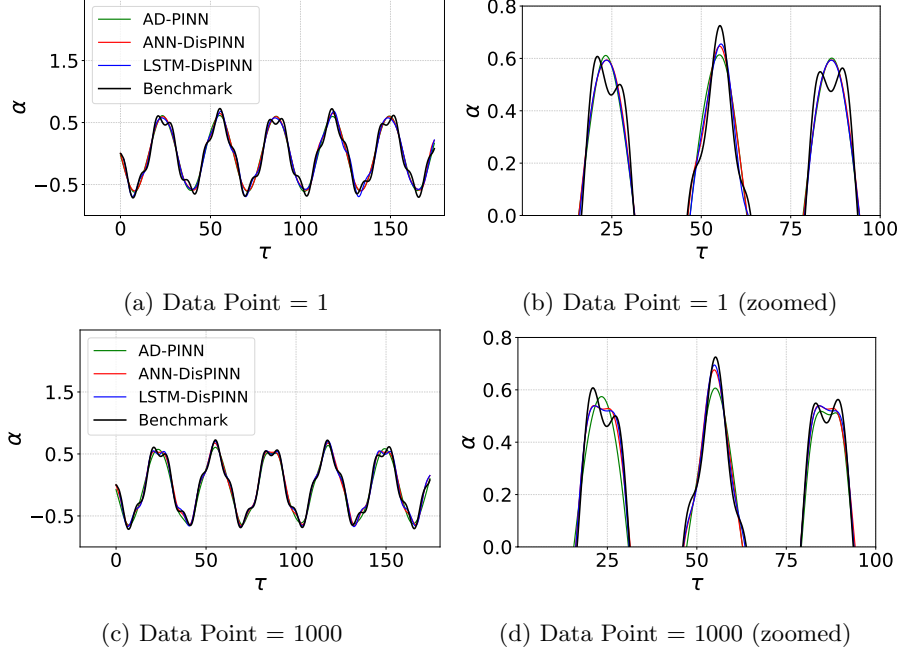


Figure 7: Comparison of the AD-PINN, LSTM-DisPINN and ANN-DisPINN prediction of the pitch response with benchmark numerical data

$$\text{relative error} = \frac{\sqrt{\sum_{N_t} (y_{\text{pred}} - y_{\text{actual}})^2}}{\sqrt{\sum_{N_t} (y_{\text{actual}})^2}}, \quad (27)$$

where,  $y_{\text{pred}}$  is the prediction from the surrogate model whereas the  $y_{\text{actual}}$  is the high-fidelity results at every time instants. For the ANN network (with and without the physics constraints),  $N_t = 1000$ , whereas for the LSTM network (with and without the physics constraints),  $N_t = 990$ . We have conducted neural network training 5 times keeping the number of data points the same at each run but changing the temporal locations of the data points to assess the maximum, minimum and the mean relative error associated with those 5 different runs. In those 5 different training iterations, the data point(s) are selected randomly from the temporal domain and hyper-parameters are kept the same. We compute the mean, maximum, and minimum of the relative errors corresponding to the 5 different training runs, which are termed as  $E_{\text{mean}}$ ,  $E_{\text{max}}$  and  $E_{\text{min}}$ , respectively.

As noticed there, for a very sparse training dataset when 1 and 3 randomly chosen high-fidelity data points are available in the temporal domain, both ANN and LSTM network without any physics information, produces large  $E_{\text{mean}}$ , whereas, AD-PINN, ANN-DisPINN and LSTM-DisPINN produce significantly accurate results. The  $E_{\text{mean}}$  associated with the plunge response corresponding to ANN and LSTM networks is 1.01 and 0.84 for data-point 1 and 0.92, 0.88 for 3 data points. However, when the physics-based loss term is added to the data-driven loss term, with only 1 data point, the  $E_{\text{mean}}$  decreases to 0.22 for AD-PINN and 0.18 and 0.16 for ANN-DisPINN and LSTM-DisPINN. The  $E_{\text{max}}$  and  $E_{\text{min}}$  associated with the ANN and LSTM network show that with the changes in the positions of the data points, prediction error associated with both networks can vary over a wide range as shown in Figure 8a and Figure 8b. However, with the addition of the physics constraints, LSTM-DisPINN performs better than the ANN-DisPINN with 1 and 3 data points. The average relative error associated with AD-PINN is comparatively higher than ANN-DisPINN and LSTM-DisPINN for all the data-points. For the pitch responses, the trends are similar, as shown in Figure 8c and Figure 8d. However, as we increase the number of data points, the prediction accuracy associated with the data-driven networks (ANN and LSTM) is close to that associated with the discretized physics-driven neural networks. Furthermore, at 200 data points, an almost similar trend of data points 1 and 3 are followed, such as LSTM-DisPINN outperforms ANN-DisPINN at all 5 training iterations and  $E_{\text{mean}}$ s associated with the

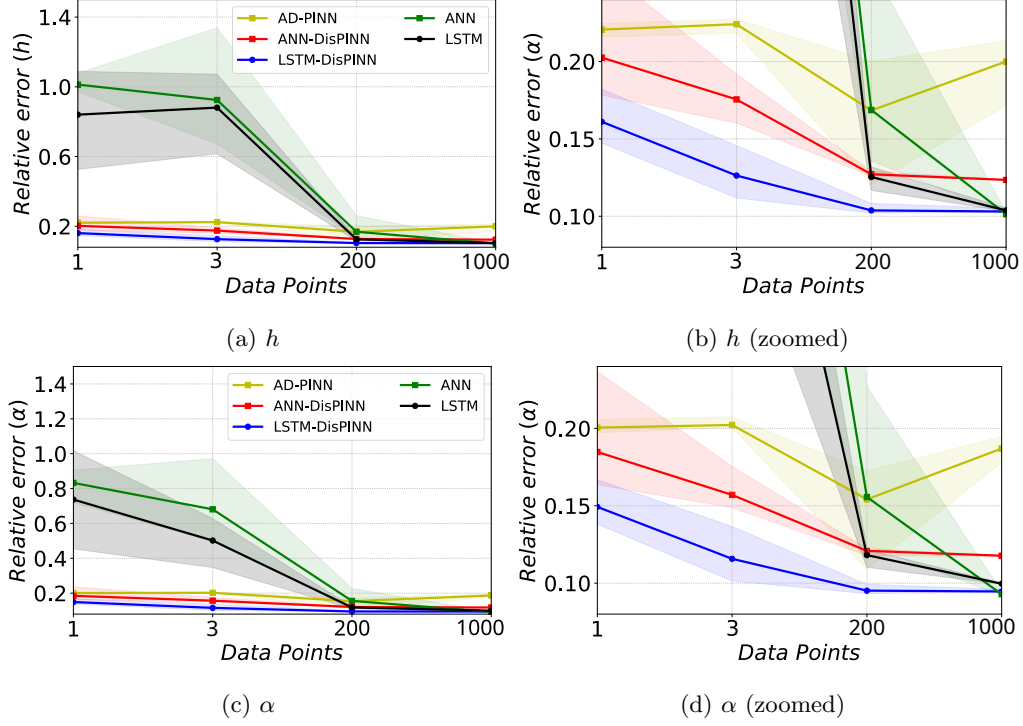


Figure 8: Comparison of the relative errors of prediction of the plunge and pitch response using Data-Driven and different PINN approach.

ANN and LSTM network are above the ones corresponding to discretized physics-constrained networks. However,  $E_{mean}$  associated with the purely data-driven LSTM network is higher than the AD-PINN. Conversely, when all the datasets are used in the PINN framework, the data-driven LSTM and ANN network work slightly better than the discretized-physics-driven PINN network. A similar trend is also followed in the pitch responses case. In conclusion, these observations show that when a sparse dataset is available, a discretized-physics-informed neural network shows its potential over a purely data-driven network. On the contrary, when a large dataset is available, a purely data-driven approach is enough to predict the system dynamics. Adding the physics-based loss term increases the magnitude of the residual of the network at each iteration or epoch of the optimization algorithm. The additional computational burden arising from the physics-based residual often causes the loss value to get stuck at an intermediate level if the optimization algorithm in the network is not properly tuned. Hence, the pure data-driven neural network may outperform the physics-constrained neural network when a large dataset is available. The authors like to mention that the error shown here corresponds to the hyper-parameters mentioned previously. Therefore, the performances of different networks may alter with different hyper-parameters.

So far, we have demonstrated the potential of the discretized governing equation-based PINN for the reconstruction of a time series with available numerical data points at selected locations of the temporal domain, whereas the residual arising from the discretized governing equations are minimized at all the time instants. To check such networks' prediction capability, governing equations are solved at initial time instants in addition to numerical data points selected within the initial time instants. The pitch and plunge responses are now predicted at the future time instants. Figure 9 shows the prediction capability of the ANN-DisPINN and LSTM-DisPINN network and compares them with the benchmark high-fidelity data. Figure 9a, Figure 9b and Figure 9c show the prediction capability when first 5, 50, and 500 time-instants are used for the residual-minimization arising from the discretized equation and only the first time instant in the temporal domain is considered for the data-driven loss term. No additional data points are selected other than the data-driven constraints arising from the initial condition.

As shown in Figure 9a, with 5 points used for discretized equation, both the ANN-DisPINN and LSTM-DisPINN show the large relative errors of 0.97 and 1.07 as indicated in Table 1. However, as we increase the training points where the equations are solved in 50 temporal instants, shown in

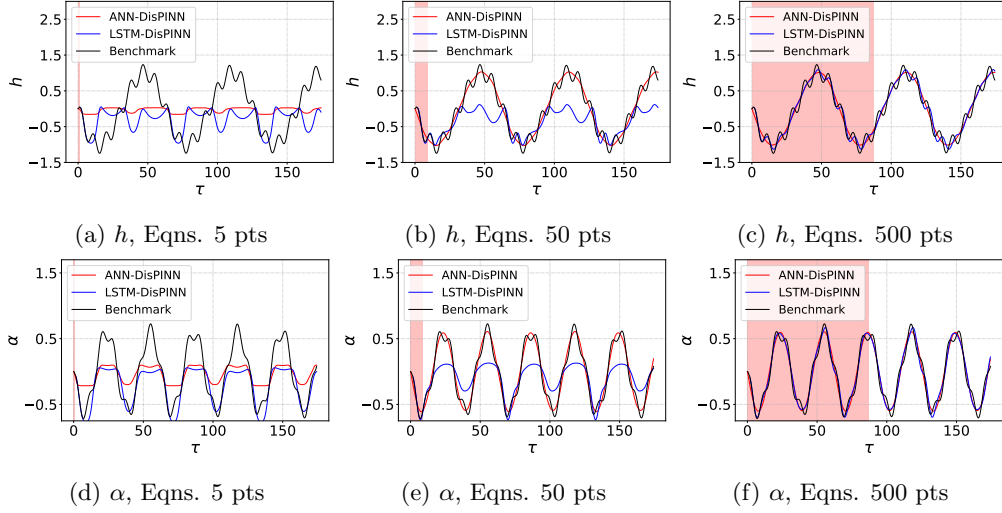


Figure 9: Comparison of the LSTM-DisPINN and ANN-DisPINN prediction of the plunge and pitch response with benchmark numerical data where equations solved in internal spatiotemporal points and only initial data ( $=1$ ) used.

Figure 9b, the ANN-DisPINN can predict the trend of the pitch and plunge responses generating an error of 0.20 whereas the error associated with the LSTM-DisPINN is still very large, 0.78. Conversely, at 500 points, as noticed in Figure 9c, the error associated with the ANN network does not change significantly, whereas the prediction error associated with the LSTM network drops to 0.20 demonstrating the prediction capability of discretized equation-based networks with only one numerical data point considered at the initial time instant. As shown in Figure 9c, the LSTM-DisPINN network has been able to predict the high-frequency responses, whereas the ANN-DisPINN fails.

Eqns Solved	ANN-DisPINN	LSTM-DisPINN
5	0.97	1.07
50	0.20	0.78
500	0.22	0.20

Table 1: Prediction error associated with the ANN-DisPINN and LSTM-DisPINN for plunge response

## 4.2 Burgers' Equation

The Burgers' equation is used as a test case to demonstrate the potential of our approaches to spatiotemporal problems. In the current subsection, the full-order discretized equation is considered in the loss term of the ANN and LSTM network in addition to the data-driven loss term. To develop the surrogate model for the Burgers' equation, 4 layers with 124, 64, 24 and 8 neurons are considered. The ANN network's learning rate is 0.006, and the number of epochs is 6000. In the case of the LSTM network, similar to the mass-spring system, sequence length is considered as 10. The number of neurons in each layer is taken as 10. The learning rate of the LSTM network is considered 0.1, and the number of epochs is 6000. Furthermore, in the following subsection 4.3, we will show the application of the reduced-order discretized equation obtained after the POD-Galerkin projection of the full-order system as shown in Equation 8 followed by integration with data-driven ANN and LSTM network as shown in Figure 2 and Figure 3. We first assess the accuracy of the conventional PINN framework, where an ANN-based neural network is coupled with the governing equations, where the derivatives are computed using automatic differentiation. The predicted results are compared with the high-fidelity results, where the convective and diffusive parts of the equation are computed using numerical schemes demonstrated in Equation 12. For the generation of the high-fidelity database, the temporal domain is discretized into 100 time steps,



whereas the spatial domain is discretized into a 20 equally spaced domain. Figure 10 shows the high-fidelity results, distribution of the spatiotemporal variable arising from the surrogate model, and associated absolute error distribution between the prediction and ground truth. The automatic differentiation-based derivative requires both the space and time variables as input of the neural network to compute the gradient terms. Therefore, the size of the input of the conventional PINN is  $\mathbb{R}^{2000 \times 2}$  where the size of the output variable  $u$  is  $\mathbb{R}^{2000 \times 1}$  which corresponds to the spatio-temporal domain ( $x$  and  $t$ ) mentioned in the input. In figure Figure 10, different sizes of training datasets are considered i.e. the number of the data point is 1 as shown in Figure 10(a) and all the data points which are 1000 shown in Figure 10(b).

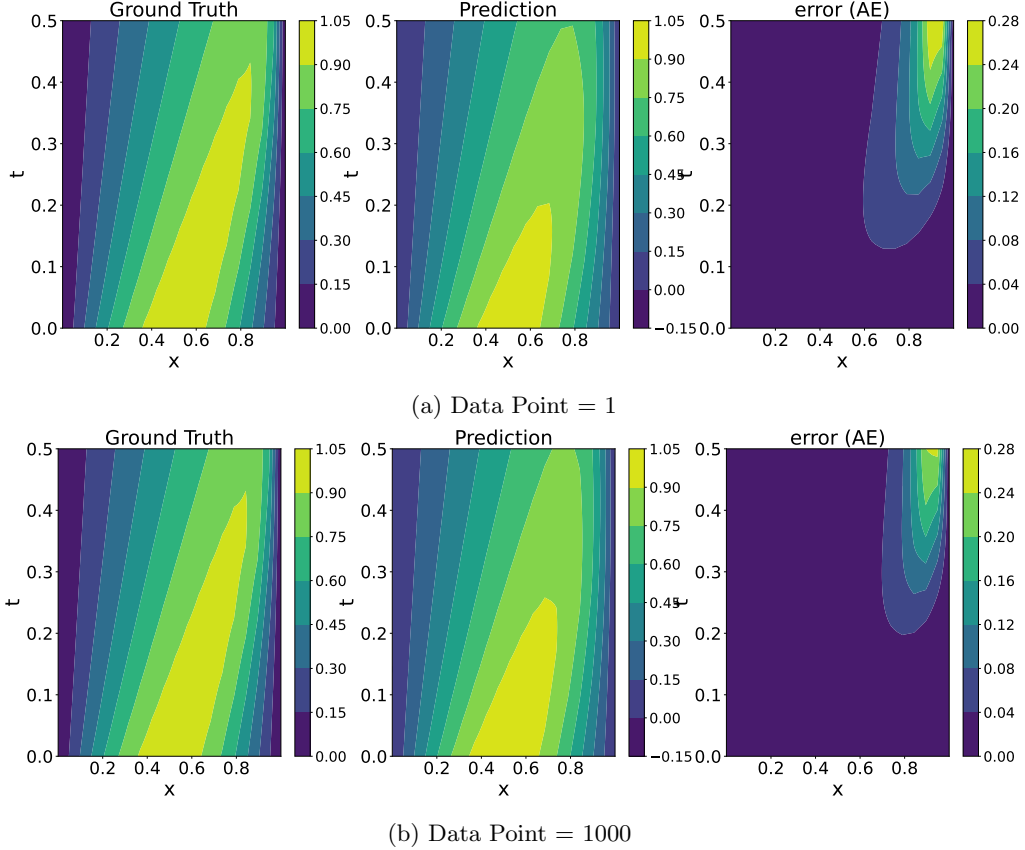


Figure 10: Comparison of the AD-based conventional PINN prediction with different number of data points used.

The data points in Figure 10(a) are chosen randomly from the spatio-temporal domain. Apart from the data-driven loss term arising from the data point, the initial conditions,  $u(x, 0) = 0$ , and boundary conditions,  $u(0, t) = u(L, t) = 0$  are enforced in the data-driven loss part of the PINN network. However, the physics-based loss terms arising from governing equations are computed at 100 random locations in the spatio-temporal domain. The benchmark or the high-fidelity results are computed using a numerical scheme where the computation of the derivative is very different from the one adopted in the PINN network (AD-based derivative). Therefore, the data-driven loss term does not comply with the physics-based loss term thereby resulting in a large deviation of the surrogate model with respect to the high-fidelity model as shown at the end of the  $x$ -location and  $t$ -domain or the north-right corner of the error (AE) of Figure 10(a) and Figure 10(b). The maximum error associated with the conventional PINN, when only 1 and full datasets are available, are respectively 0.2726 and 0.25 as indicated in Table 2. However, gain in accuracy is not achieved much as we increase the number of data points in the training set because the major source of error is the no-compatibility of the AD-based derivative and numerical derivative, which produced the dataset initially and not the sparse data point. Now, we introduce the application of discretized governing equation-based loss function in the PINN network with the ANN and LSTM network. As mentioned previously, conventional PINN computes the derivative using automatic differentiation,

which requires the spatio-temporal coordinates ( $x$  and  $t$ ) as inputs. However, our approach of using discretized governing equation-based PINN offers the flexibility of choice of network input. For example, in the current work, only the time instants, i.e., 100 time steps are considered as the network input. The  $u$  variables at 20 grid points are considered as the output. Therefore for the ANN network, the input size is  $\mathbb{R}^{(100 \times 1)}$  whereas the output dimension is  $\mathbb{R}^{(100 \times 20)}$ . In Figure 11 and Figure 12 the error associated with ANN-DisPINN and LSTM-DisPINN is compared with a comprehensive data-driven ANN and LSTM network.

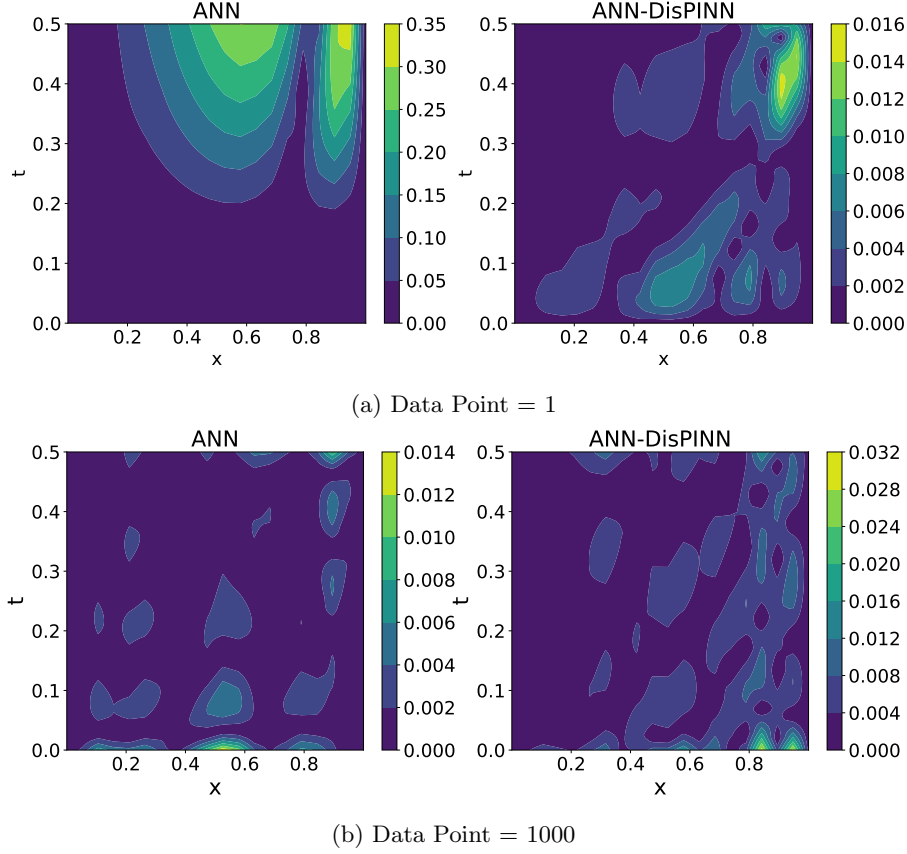


Figure 11: Absolute error associated with the ANN and ANN-DisPINN with different Data points used.

The error associated with discretized governing equation-based ANN-DisPINN is much lower than the conventional PINN network as shown in Figure 10. Furthermore, the training time is greatly reduced since the temporal domain is only considered as an input instead of both space ( $x$ ) and time ( $t$ ) variables. It shows, similar to the Mass-spring system, the potential of the ANN-DisPINN and LSTM-DisPINN as compared to the complete data-driven ANN and LSTM ROM when a very sparse dataset is available. When one training data point is only available, the maximum error associated with the data-driven ANN network is 0.35 whereas, with the ANN-DisPINN network with the discretized equation is 0.016, indicated in Table 2. However, when all the data points are used, the maximum error incurred with the ANN network is 0.014, whereas with the ANN-DisPINN network is 0.032 and thereby supporting the conclusion we made in the earlier section on the mass-spring system - when a large dataset is available, purely data-driven ROM tends to outperform the disPINN or AD-PINN. While using the LSTM network, a sequence length of 10 and neuron size of 10 in each LSTM cell is used. As shown in the Figure 3, input is first reshaped into the sequence windows to get the tensor structure, and the length of the spatio-temporal series becomes 90, corresponding to the 90 output. In the case of one data point, as shown in Figure 12a, the maximum error associated with the data-driven LSTM and discretized-physics-driven LSTM networks is 0.2154 and 0.011. However, when all the data points are used, both the error is  $\approx 0.008$ . The errors are indicated in Table 2.

Now, we assess the applicability of the discretized equation-based ANN and LSTM network

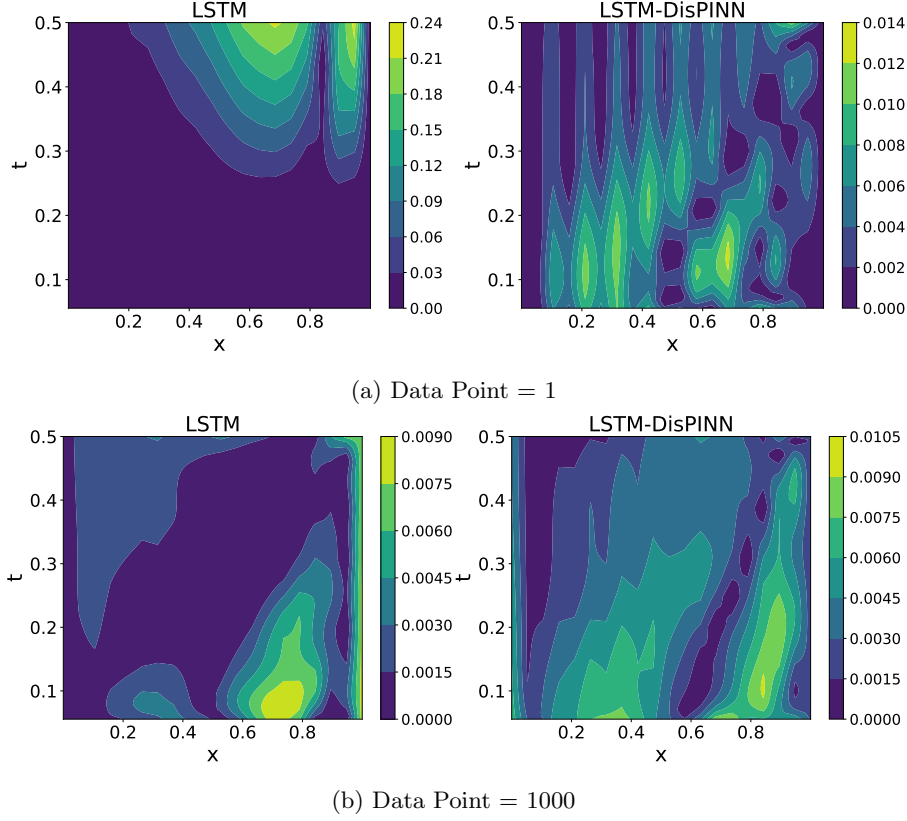


Figure 12: Absolute error associated with the LSTM and LSTM-DisPINN with different Data points used.

Data-Points	AD-PINN	ANN-DisPINN	LSTM-DisPINN	ANN	LSTM
1	0.27	0.016	0.011	0.35	0.2154
1000	0.25	0.032	0.008	0.014	0.008

Table 2: Maximum absolute error associated with the ANN-DisPINN and LSTM-DisPINN for Burgers' equation.

for prediction at future time steps while the numerical data points and governing equations-based residual minimization are considered only within a few initial time-instants. For the ANN network, we minimize the discretized equation-based residual from  $2^{nd}$  time step to  $12^{nd}$  time step and from  $2^{nd}$  time step to  $52^{nd}$  time step with a total of 10 and 50 time steps respectively. The initial condition  $u = u_{int}$  is the only data-driven constraint considered in the ANN-DisPINN network. As shown in Figure 13a, when the discretized governing equation Equation 12 are minimized in the initial 10 points, the maximum error that occurred in the spatio-temporal domain is 0.35, whereas in the case of the 50 initial points, the maximum error value is 0.175. However, in the case of the LSTM-DisPINN network, we have considered the first 10 time instants as the sequence length. Therefore, the discretized governing equation-based residuals are minimized from the  $12^{th}$  to  $22^{nd}$  and from  $12^{th}$  to  $62^{nd}$  time-step as shown in Figure 13b. The  $u$  value at the  $10^{th}$  timesteps is considered as the data-driven constraint in the LSTM-DisPINN network. With 10 and 50 time steps, the maximum absolute errors are 0.48 and 0.105. Although with LSTM-DisPINN the network prediction accuracy has been improved over the ANN-DisPINN when 50 time steps are considered, the prediction capability is poorer than the reconstruction capability demonstrated previously where the discretized equation-based residuals are minimized in the entire temporal domain. The prediction capability in terms of absolute error with respect to the benchmark high-fidelity data is demonstrated in Table 3.

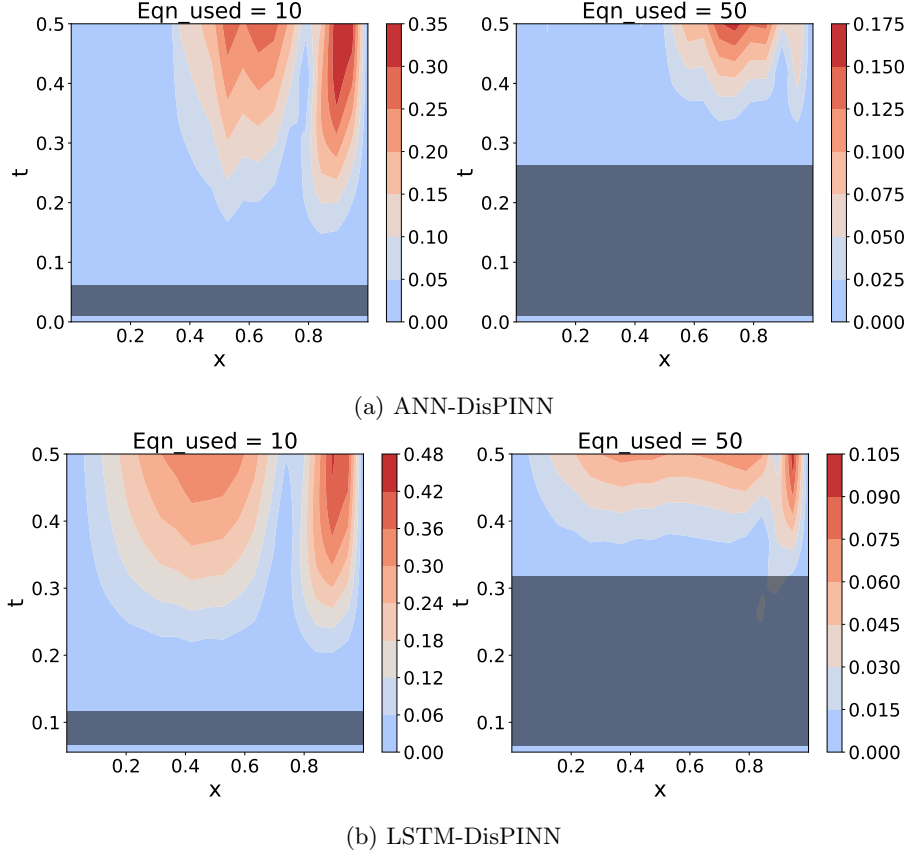


Figure 13: Error associated with prediction capabilities when equations solved in the internal spatio-temporal domain and numerical initial point data (=1) used.

Eqns Solved	ANN-DisPINN	LSTM-DisPINN
10	0.35	0.175
50	0.48	0.10

Table 3: Prediction error associated with the ANN-DisPINN and LSTM-DisPINN for the Burgers' Equation.

### 4.3 Reduced Order Burgers' Equation

In this current section, we first carry out the POD-Galerkin projection of the Burgers' equation in discretized form, followed by the inclusion of discretized reduced order equation in the PINN network. 10 POD modes and 10 DEIM control points are considered in the current work. Similar to the previous subsection 4.2, the entire temporal domain, which is 100 time instants, is considered as the input to the neural network. Conversely, in the output, instead of the full discretized equation Equation 12, only the reduced order Equation 13 are considered. Non-linearity arising from the convection term is handled using hyper-reduction as shown in Equation 17. Therefore, computational training time savings are achieved. First, the solution vectors at different time instants are considered. Then SVD is applied to the set of solution vectors to compute the POD modes. The reconstruction error is defined as the absolute error between the high-fidelity results and the reconstructed field from the POD coefficients. The reconstruction error is computed with a different number of modes such as 2, 5 and 10 as shown in Figure 14. The maximum error associated with 2, 5 and 10 number of modes are 0.175, 0.004 and  $10^{(-6)}$  respectively. In the context of a discretized reduced order system-based PINN framework, the reconstruction error first needs to be minimized to expect an overall minimization of error. Hence 10 modes are considered for the PINN prediction. Figure 15a and Figure 15b show the prediction of the PINN network using discretized reduced order governing equation and employing ANN and LSTM as a neural

network, respectively. As previously noticed, the LSTM-PINN network outperforms the ANN-PINN network since the maximum error associated with the LSTM-DisPINN and ANN-DisPINN are 0.014 and 0.032, respectively, when sparse datasets such as data-point of 1 are considered, and discretized-equation-based residual is minimized in the entire computational domain. However, with the increment of the data points (i.e. 1000 for ANN-DisPINN and 990 for LSTM-DisPINN), the maximum absolute error drops to 0.016 and 0.0090, respectively. Table 4 shows the wall clock time required for the training using the full order and reduced order ANN-DisPINN and LSTM-DisPINN while using the 10 and 5 DEIM control points and POD modes respectively. It is evident from Table 4, that when the number of modes is reduced to 10 and 5 which is half and a quarter of the total grid size, the computational time is not linearly reduced. Parametric variation and temporal prediction in a future time step will be considered as a future endeavour by the authors to investigate the full potential of the reduced-order discretized physics-based network. Although we intend to reduce the usage of numerical data in ANN-DisPINN and LSTM-DisPINN to demonstrate the potential use of PINN, in the projection phase (POD-Galerkin projection) we have considered the full spatio-temporal domain for the computation of the POD modes and DEIM control points. The authors also aim to reduce the requirements of numerical data in the projection phase using discretized physics-based convolution autoencoder [36] as a future extension of the current work.

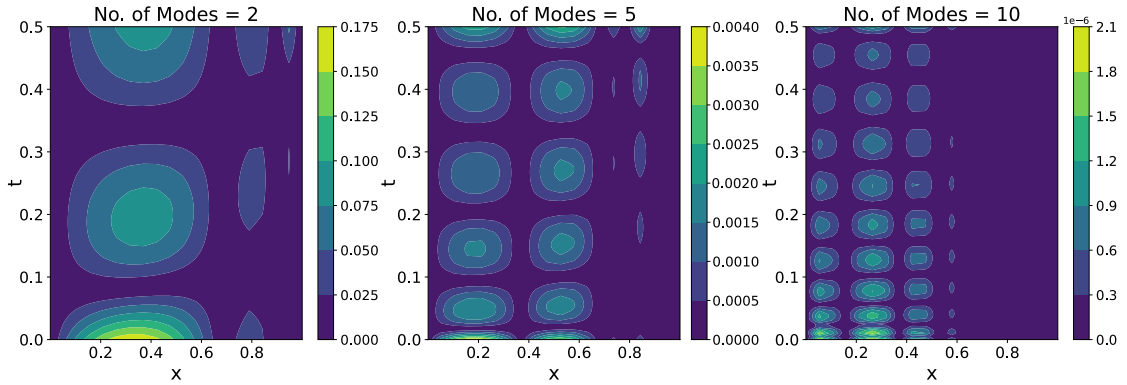


Figure 14: Absolute error associated with the reconstruction with different numbers of POD basis used.

No. of Modes and DEIM pts.	ANN-DisPINN	ANN-DisPINN Reduced
10	1111.65 <i>s</i>	937.60 <i>s</i>
5	1111.65 <i>s</i>	561.99 <i>s</i>
No. of Modes and DEIM pts.	LSTM-DisPINN	LSTM-DisPINN Reduced
10	993.40 <i>s</i>	852.03 <i>s</i>
5	993.40 <i>s</i>	521.52 <i>s</i>

Table 4: Time taken for different full order (ANN-DisPINN and LSTM-DisPINN) and Reduced Order (ANN-DisPINN and LSTM-DisPINN) training.

#### 4.4 Coupling with Detached External Solver

In this subsection, we will discuss the inclusion of the discretized form of the governing equation in the computational graph of the network using the steps mentioned in subsection 4.4 and algorithm 1, when the external solver is completely detached from the PINN environment. The external Burgers' equation although implemented in the PyTorch platform, we ensured while passing the residual and the Jacobian,  $J$  to the PINN solver, they are detached from the computational graph. This is to ensure, potential coupling with any external solver. Figure 16 demonstrates that for ANN-DisPINN, if  $J$  is updated at 100, 500, 1000 epochs interval, the governing equation-based residual  $MSE_{\text{burgers}}$  is minimized ensuring the accuracy of the solution at an insignificant increment of the training time. The residual minimization is similar to the case mentioned in

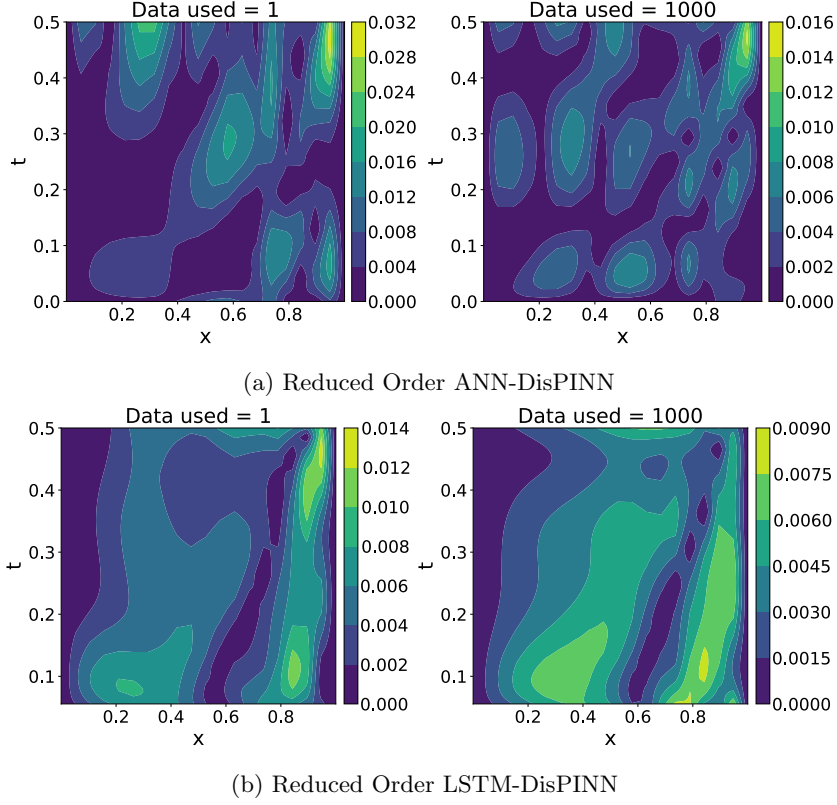


Figure 15: Error associated with the reduced order ANN-DisPINN and LSTM-DisPINN with different data points used.

subsection 4.2, where the functional form of the discretized equation is not detached from the computational graph (indicated by black solid lines and termed as w/o loss term modification). If the Jacobian  $J$  is updated at an interval of 2000, in the case of the ANN-DisPINN, the loss term starts increasing after approximately 800 time-steps. Although the Jacobian update step is expensive, since it is updated only at a few epoch intervals, the total training time is not affected significantly while maintaining the solution accuracy as shown in Figure 17. Furthermore, in the case of the LSTM-DisPINN, the physics-based loss term is minimized even with 2000 epoch interval of the  $J$  update. The absolute error associated with the Burgers' equation is shown using our proposed new loss term with a Jacobian  $J$  update of 500 and 100 epoch interval for the ANN-DisPINN and LSTM-DisPINN respectively and the prediction is in good agreement with the benchmark numerical results. The hyper-parameter for the ANN-DisPINN and LSTM-DisPINN is kept similar as mentioned in the subsection 4.2. Only the initial condition which is timestep = 0 for ANN-DisPINN and timestep = 10 for LSTM-DisPINN is considered for the data-driven loss term in algorithm 1.

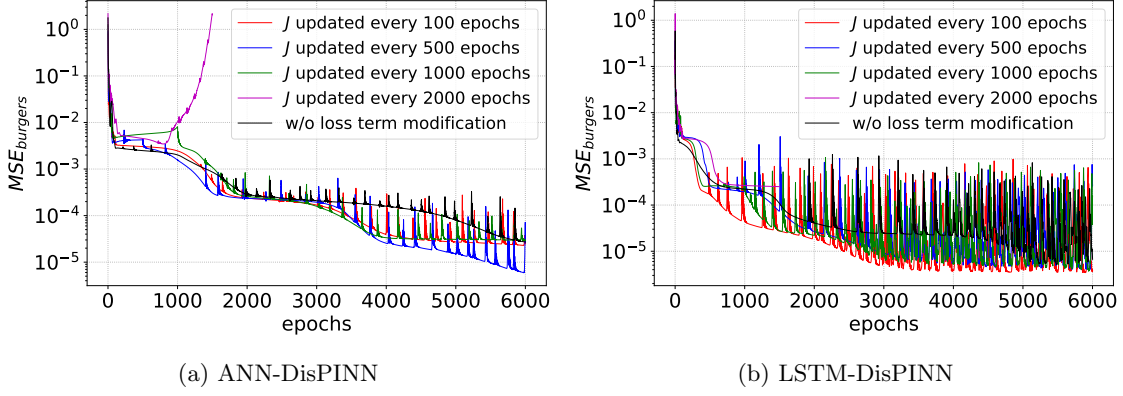


Figure 16: mse associated with the Physics-based loss term with a number of epochs and different jacobian,  $J$  update rate.

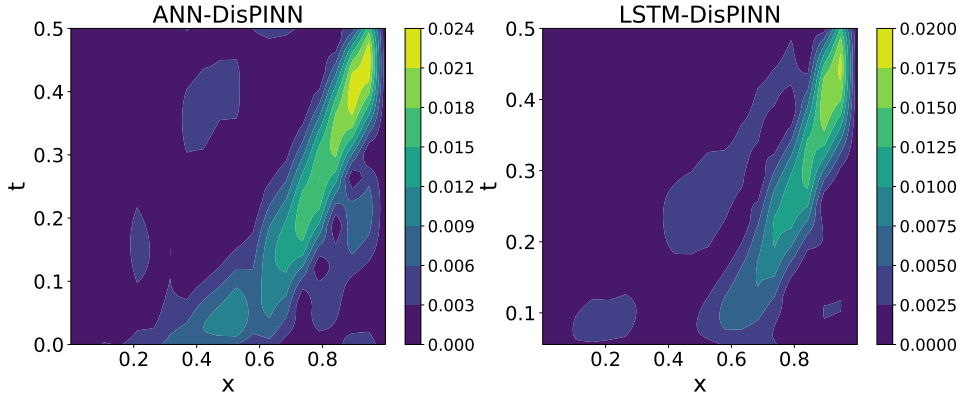


Figure 17: Comparison of the error associated with the ANN-DisPINN and LSTM-DisPINN after new loss term ( $L_{Dis}$ ) modification (Data used = 1).

## 5 Conclusion

In this current work, we propose a novel scheme introducing the discretized governing equations followed by a POD-Galerkin projection of the discretized governing equation and using the numerical residuals in the loss term of the ANN and LSTM network. The proposed approach shows its potential over the conventional Automatic Differentiation-based physics-informed neural network and also lays the foundation for applications in coupling with external forward solvers. The LSTM-PINN network, given an architecture-dependent on the time history of input, possesses several difficulties in terms of the conventional PINN framework. Still, in the current framework, any type of neural network including the LSTM network can be put easily. The additional projection of discretized governing equations onto reduced space improves the training time without compromising the prediction accuracy. Our recent work also demonstrates that if the training dataset is large, the pure data-driven network outperforms the physics-constrained ROM. The introduction of the physics-based loss term appears to deteriorate the performance by increasing the magnitude of the residual. We also propose an efficient algorithm for coupling forward solvers with PINN where it is difficult to access the discretized form of the equation to include them in the computational graph without a significant increase in training time. In future, open-source forward CFD platforms or software dedicated to handling projection-based reduced order schemes will be coupled with the physics-informed neural network framework for complex geometry and large-scale problems.

## Data Availability

The data sets generated during and/or analyzed during the current study are available from the corresponding authors upon reasonable request.



## Disclosure Statement

The authors report no potential conflict of interest.

## Acknowledgements

The authors gratefully acknowledge the financial support under the scope of the COMET program within the K2 Center “Integrated Computational Material, Process and Product Engineering (IC-MPPE)” (Project No 886385). This program is supported by the Austrian Federal Ministries for Climate Action, Environment, Energy, Mobility, Innovation and Technology (BMK) and for Labour and Economy (BMAW), represented by the Austrian Research Promotion Agency (FFG), and the federal states of Styria, Upper Austria, and Tyrol. The authors also acknowledge financial support from MUR PRIN project NA\_FROM\_PDEs, INDAM GNCS and MUR PRIN project ROMEU.

## References

- [1] Shun-ichi Amari. Backpropagation and stochastic gradient descent method. *Neurocomputing*, 5(4-5):185–196, 1993.
- [2] Deepinder Jot Singh Aulakh, Steven B Beale, and Jon G Pharoah. A generalized framework for unsupervised learning and data recovery in computational fluid dynamics using discretized loss functions. *Physics of Fluids*, 34(7):077111, 2022.
- [3] Maxime Barrault, Yvon Maday, Ngoc Cuong Nguyen, and Anthony T Patera. An ‘empirical interpolation’ method: application to efficient reduced-basis discretization of partial differential equations. *Comptes Rendus Mathematique*, 339(9):667–672, 2004.
- [4] Atilim Gunes Baydin, Barak A Pearlmutter, Alexey Andreyevich Radul, and Jeffrey Mark Siskind. Automatic differentiation in machine learning: a survey. *Journal of Machine Learning Research*, 18:1–43, 2018.
- [5] P. Benner, S. Grivet-Talocia, A. Quarteroni, G. Rozza, W. Schilders, and L. M. Silveira. *System-and Data-Driven Methods and Algorithms*. De Gruyter, 2021.
- [6] Peter Benner, Serkan Gugercin, and Karen Willcox. A Survey of Projection-Based Model Reduction Methods for Parametric Dynamical Systems. *SIAM Review*, 57(4):483–531, 2015.
- [7] Peter Benner, Wil Schilders, Stefano Grivet-Talocia, Alfio Quarteroni, Gianluigi Rozza, and Luís Miguel Silveira. *Model order reduction: volume 3 applications*. De Gruyter, 2020.
- [8] Umair bin Waheed, Ehsan Haghighat, Tariq Alkhalifah, Chao Song, and Qi Hao. PIN-Neik: Eikonal solution using physics-informed neural networks. *Computers & Geosciences*, 155:104833, 2021.
- [9] Kevin Carlberg, Charbel Farhat, Julien Cortial, and David Amsallem. The GNAT method for nonlinear model reduction: effective implementation and application to computational fluid dynamics and turbulent flows. *Journal of Computational Physics*, 242:623–647, 2013.
- [10] S. Chaturantabut and D.C. Sorensen. Nonlinear Model Reduction via Discrete Empirical Interpolation. *SIAM Journal on Scientific Computing*, 32(5):2737–2764, 2010.
- [11] Wenqian Chen, Qian Wang, Jan S. Hesthaven, and Chuhua Zhang. Physics-informed machine learning for reduced-order modeling of nonlinear problems. *Journal of Computational Physics*, 446:110666, 2021.
- [12] Chen Cheng and Guang-Tao Zhang. Deep learning method based on physics informed neural network with resnet block for solving fluid flow problems. *Water*, 13(4):423, 2021.
- [13] Dario Coscia, Anna Ivagnes, Nicola Demo, and Gianluigi Rozza. Physics-Informed Neural networks for Advanced modeling. *Journal of Open Source Software*, 8(87):5352, 2023.



- [14] Salvatore Cuomo, Vincenzo Schiano Di Cola, Fabio Giampaolo, Gianluigi Rozza, Maziar Raissi, and Francesco Piccialli. Scientific machine learning through physics-informed neural networks: where we are and what's next. *Journal of Scientific Computing*, 92(3):88, 2022.
- [15] N. Demo, M. Tezzele, G. Gustin, G. Lavini, and G. Rozza. Shape optimization by means of proper orthogonal decomposition and dynamic mode decomposition. *Technology and Science for the Ships of the Future: Proceedings of NAV 2018: 19th International Conference on Ship & Maritime Research*, page 212–219, 2018.
- [16] N. Demo, M. Tezzele, A. Mola, and G. Rozza. A complete data-driven framework for the efficient solution of parametric shape design and optimisation in naval engineering problems. *arXiv preprint arXiv:1905.05982*, 2019.
- [17] Nicola Demo, Maria Strazzullo, and Gianluigi Rozza. An extended physics informed neural network for preliminary analysis of parametric optimal control problems. *Computers & Mathematics with Applications*, 143:383–396, 2023.
- [18] MWMG Dissanayake and Nhan Phan-Thien. Neural-network-based approximations for solving partial differential equations. *communications in Numerical Methods in Engineering*, 10(3):195–201, 1994.
- [19] Zhiwei Fang and Justin Zhan. A physics-informed neural network framework for PDEs on 3D surfaces: Time independent problems. *IEEE Access*, 8:26328–26335, 2019.
- [20] Charbel Farhat, Todd Chapman, and Philip Avery. Structure-preserving, stability, and accuracy properties of the energy-conserving sampling and weighting method for the hyper reduction of nonlinear finite element dynamic models. *International journal for numerical methods in engineering*, 102(5):1077–1110, 2015.
- [21] Mahmoud Gadalla, Marta Cianferra, Marco Tezzele, Giovanni Stabile, Andrea Mola, and Gianluigi Rozza. On the comparison of LES data-driven reduced order approaches for hydroacoustic analysis. *Computers & Fluids*, 216:104819, 2021.
- [22] Han Gao, Luning Sun, and Jian-Xun Wang. PhyGeoNet: Physics-informed geometry-adaptive convolutional neural networks for solving parameterized steady-state PDEs on irregular domain. *Journal of Computational Physics*, 428:110079, 2021.
- [23] R. Halder, M. Damodaran, and B.C. Khoo. Deep Learning Based Reduced Order Model for Airfoil-Gust and Aeroelastic Interaction. *AIAA Journal*, 58(10):1–18, 2020.
- [24] Rahul Halder, Murali Damodaran, and Boo Cheong Khoo. Computational Assessment of Transonic Airfoil-Gust Aeroelastic Response. *AIAA Journal*, 60(4):2597–2614, 2022.
- [25] Rahul Halder, Murali Damodaran, and BC Khoo. Deep learning-driven nonlinear reduced-order models for predicting wave-structure interaction. *Ocean Engineering*, 280:114511, 2023.
- [26] Saddam Hijazi, Melina Freitag, and Niels Landwehr. POD-Galerkin reduced order models and physics-informed neural networks for solving inverse problems for the Navier–Stokes equations. *Advanced Modeling and Simulation in Engineering Sciences*, 10(1):1–38, 2023.
- [27] Efthymios N. Karatzas, Giovanni Stabile, Leo Nouveau, Guglielmo Scovazzi, and Gianluigi Rozza. A Reduced-Order Shifted Boundary Method for Parametrized incompressible Navier-Stokes equations. *Computer Methods in Applied Mechanics and Engineering*, 370:113273, 2020.
- [28] Pradeepa T. Karnick and Kartik Venkatraman. Shock–boundary layer interaction and energetics in transonic flutter. *Journal of Fluid Mechanics*, 832:212–240, 2017.
- [29] Hugo FS Lui and William R Wolf. Construction of reduced-order models for fluid flows using deep feedforward neural networks. *Journal of Fluid Mechanics*, 872:963–994, 2019.
- [30] Romit Maulik, Omer San, Adil Rasheed, and Prakash Vedula. Subgrid modelling for two-dimensional turbulence using neural networks. *Journal of Fluid Mechanics*, 858:122–144, 2019.

- [31] Eric J Parish and Karthik Duraisamy. A paradigm for data-driven predictive modeling using field inversion and machine learning. *Journal of computational physics*, 305:758–774, 2016.
- [32] Alfio Quarteroni, Andrea Manzoni, and Federico Negri. *Reduced basis methods for partial differential equations: an introduction*, volume 92. Springer, 2015.
- [33] Sk M Rahman, Suraj Pawar, Omer San, Adil Rasheed, and Traian Iliescu. Nonintrusive reduced order modeling framework for quasigeostrophic turbulence. *Physical Review E*, 100(5):053306, 2019.
- [34] M. Raissi, P. Perdikaris, and G.E. Karniadakis. Physics-informed neural networks: A deep learning framework for solving forward and inverse problems involving nonlinear partial differential equations. *Journal of Computational Physics*, 378(1):686–707, 2019.
- [35] Rishikesh Ranade, Chris Hill, and Jay Pathak. Discretizationnet: A machine-learning based solver for navier–stokes equations using finite volume discretization. *Computer Methods in Applied Mechanics and Engineering*, 378:113722, 2021.
- [36] Francesco Romor, Giovanni Stabile, and Gianluigi Rozza. Non-linear manifold reduced-order models with convolutional autoencoders and reduced over-collocation method. *Journal of Scientific Computing*, 94(3):74, 2023.
- [37] Gianluigi Rozza, Giovanni Stabile, and Francesco Ballarin. *Advanced Reduced Order Methods and Applications in Computational Fluid Dynamics*. SIAM, 2022.
- [38] Enrico Schiassi, Roberto Furfaro, Carl Leake, Mario De Florio, Hunter Johnston, and Daniele Mortari. Extreme theory of functional connections: A fast physics-informed neural network method for solving ordinary and partial differential equations. *Neurocomputing*, 457:334–356, 2021.
- [39] Jürgen Schmidhuber. Deep learning in neural networks: An overview. *Neural networks*, 61:85–117, 2015.
- [40] Giovanni Stabile, Saddam Hijazi, Andrea Mola, Stefano Lorenzi, and Gianluigi Rozza. POD-Galerkin reduced order methods for CFD using Finite Volume Discretisation: vortex shedding around a circular cylinder. *Communications in Applied and Industrial Mathematics*, 8(1):210–236, 2017.
- [41] Giovanni Stabile and Gianluigi Rozza. Finite volume POD-Galerkin stabilised reduced order methods for the parametrised incompressible Navier–Stokes equations. *Computers & Fluids*, 173:273–284, 2018.
- [42] Giovanni Stabile, Matteo Zancanaro, and Gianluigi Rozza. Efficient Geometrical parametrization for finite-volume based reduced order methods. *International Journal for Numerical Methods in Engineering*, 121(12):2655–2682, 2020.
- [43] Alexandre M Tartakovsky, C Ortiz Marrero, Paris Perdikaris, Guzel D Tartakovsky, and David Barajas-Solano. Physics-informed deep neural networks for learning parameters and constitutive relationships in subsurface flow problems. *Water Resources Research*, 56(5):e2019WR026731, 2020.
- [44] Zheng Wang, Dunhui Xiao, Fangxin Fang, Rajesh Govindan, Christopher C Pain, and Yike Guo. Model identification of reduced order fluid dynamics systems using deep learning. *International Journal for Numerical Methods in Fluids*, 86(4):255–268, 2018.